Microstrip Gas Detectors and a Search for Ξ-Hypernuclei

By

Michael Robert Landry

A THESIS

SUBMITTED TO THE FACULTY OF GRADUATE STUDIES IN PARTIAL

FULFILLMENT OF THE REQUIREMENTS

FOR THE DEGREE OF

DOCTOR OF PHILOSOPHY

IN

PARTICLE & NUCLEAR PHYSICS

DEPARTMENT OF PHYSICS

THE UNIVERSITY OF MANITOBA

WINNIPEG, MANITOBA

CANADA

THE UNIVERSITY OF MANITOBA

FACULTY OF GRADUATE STUDIES

*****

COPYRIGHT PERMISSION PAGE

Microstrip Gas Detectors and a Search for Ξ-Hypernuclei

BY

Michael Robert Landry

A Thesis/Practicum submitted to the Faculty of Graduate Studies of The University of Manitoba in partial fulfillment of the requirements of the degree of Doctor of Philosophy

Abstract

A search for strangeness $S = -2$ Ξ-hypernuclei has been carried out at Brookhaven National Laboratory (BNL). Experiment 885 was conducted on the D6 beamline at the Alternating Gradient Synchrotron (AGS), using the (K^-, K^+) reaction on a diamond target at $P_{K^-} = 1.8$ GeV/c. Several novel detectors were employed, including microstrip gas chambers (MSGC) which acted as a vertex detector, and scintillating fibre (SCIFI) blocks to image decay particles. MSGC are relatively new position sensitive detectors, in which the active area of the detector is defined by a lithographed substrate, upon which electrodes are etched to collect charge from the passage of an ionizing particle. Approximately 3×10^5 (K^-, K^+) events were recorded, an order of magnitude greater than the existing world data set. Strangeness -2 hypernuclei are expected to form directly via the reaction $K^- + {}^{12}C \rightarrow {}^{12}_{\Xi} Be + K^+$. Despite limited experimental resolution (hydrogen kinematics yield 4.1 MeV/c^2 r.m.s.) that prevents resolution of discrete hypernuclear states, the missing mass spectrum was searched for evidence of bound states.

Acknowledgements

I would like to thank my thesis advisor, Willem T.H. van Oers, for his guidance and energy throughout my graduate program. My favourite image of Wim is of him following a seminar he gave, proposing a T-violation experiment. A somewhat raucous debate followed in the TRIUMF conference room, with Wim at the center of it. He came bounding into the trailer shortly after, declaring, "good for the soul".

Lawrence Lee deserves special thanks for his tireless commitment to quality, his expert tutelage in strangeness physics and good quality single-malt, and his ability to duck flying screwdrivers in the cleanroom at 3 am.

I would like to thank the members of the Manitoba group, including Des Ramsay, Charles Davis, Jim Birchall, and Shelley Page. Des and Chuck in particular were a constant source of good ideas at all phases of the experiment, from design to operation to analysis. Each were responsible for beating down several (that is, more than two) mV of RF noise in the MSGCs.

I appreciated the expert advice of Gregg Franklin and Morgan May. Thanks to Alain Berdoz, Dan Carmen and Adam Rusek for getting much of the hardware working on D-Line, and keeping it that way.

I have had the good fortune of working with a talented and intriguing cast of graduate students, particularly Kazuhiro Yamamoto, and the enigmatic Pavel Khuastov. They are a responsible for a great deal of the work on the experiment.

Other graduate students I have learned from and had the pleasure to work with include Liping Gan, Phil Koran, Kent Paschke, and Al Biglan. From Phil and Kent I learned how to maximize one's D-line angst. I'm still not certain if this is a good thing.

I would like to thank the many TRIUMF physicists and staff who helped out creating and commissioning the MSGCs, including Martin Salomon, Wayne Faszer, G. Herb Coombes, and the superb group from the Detector Facility/Scintillator Shop. Similarly, the BNL staff were a great help to me in commissioning the MSGCs; Eddie Meier and Al Minn.

Many friends provided welcome interaction and support, including Paul Distefano, Rshmi Kher, Trevor Stocki, Robert Pleydon, Rich Mawson, Ted Eickmeier, Victor Sum, and Araz Hamian.

I am especially appreciative of the patience, care and encouragement Lise has afforded me over the final stages of this program.

My brother Christopher never tired of asking about how the project was coming along, offering supportive words. My nephew Mathew is a constant source of inspiration to me; I am grateful for his love and encouragement. He drives me to try to be a better physicist.

I appreciate all the help my family gave me throughout my study. Thanks to Karen, Tom, and Joey and Roger, for all the understanding, encouragement and spontaneous financial aid.

To Marilyn, I am grateful for years of love, wisdom and support.

I cannot thank my mother and father enough for their lifelong patience, encouragement and love.

The E885 Collaboration

D.E. Alburger, R.E. Chrien, M. May, P.H. Pile, A. Rusek, R. Sawafta[1], R. Sutter
Brookhaven National Laboratory, Upton NY, USA 11973

A.R. Berdoz[2], A. Biglan[3], D.S. Carman[4], G.B. Franklin, P. Khaustov[5], P. Koran, R. Magahiz[6], R. McCrady[7], C.A. Meyer, K. Paschke, B. Quinn, R.A. Schumacher
Carnegie Mellon University, Pittsburgh PA, USA 15213

T. Bürger, H. Fischer, J. Franz, H. Schmitt
University of Freiburg, D-79104 Freiburg, Germany

T. Iijima
KEK, High Energy Accelerator Research Organization, Tsukuba, Ibaraki 305, Japan

F. Takeutchi
Kyoto Sangyo University, Kyoto 603, Japan

A. Ichikawa, K. Imai, Y. Kondo, K. Yamamoto[8], M. Yosoi
Kyoto University, Sakyo-Ku, Kyoto 606, Japan

P.D. Barnes, F. Merrill
Los Alamos National Laboratory, Los Alamos NM, USA 87545

J. Birchall, L. Gan[9], M.R. Landry, L. Lee, S.A. Page, W.D. Ramsay, W.T.H. van Oers
Department of Physics, University of Manitoba, Winnipeg MB, Canada R3T 2N2

C.A. Davis
TRIUMF, 4004 Wesbrook Mall, Vancouver BC, Canada V6T 2A3

J. Lowe
University of Birmingham, Birmingham, UK B15 2TT

B. Bassalleck, R.W. Stotzer[10]
University of New Mexico, Albuquerque NM, USA 87131

[1]Present address: North Carolina A&T State University, Greensboro, NC 27411, USA
[2]Present address: SFA Inc., Largo, MD 20774, USA
[3]Present address: Union Switch & Signal, Pittsburgh, PA 15219, USA
[4]Present address: Ohio University, Athens, OH 45701, USA
[5]Present address: Avant! Corp., Fremont, CA 94538 USA
[6]Present address: Syncsort Inc., Woodcliff Lake, NJ 07675, USA
[7]Present address: Los Alamos National Laboratory, Los Alamos, NM 87545, USA
[8]Present address: Department of Physics, Osaka City University, Osaka 558-87545, USA
[9]Present address: Hampton University, Hampton, VA 23668, USA
[10]Present address: ASAP, Albuquerque, NM 87110, USA

for Mathew

Contents

List of Figures

List of Tables

Chapter 1

Introduction

1.1 Matter and strange quarks

Brookhaven National Laboratory Experiment 885 is a search for doubly-strange (S=-2) exotic systems. The experiment is sensitive to a variety of channels for the formation of objects containing several strange quarks. This thesis is concerned with a spectrometer-based measurement of one of these channels, by looking for enhancements in an excitation spectrum indicating the formation of S=-2 Ξ-hypernuclei. In this chapter we begin by reviewing salient features in strangeness physics, such as species of interest, what experimental evidence exists for the formation of such objects, some of the physics motivations, and input from theory. An overview of E885 is then presented.

Conventional nuclei discovered to date are composed of the two lightest baryons, the proton and the neutron. In cosmic ray experiments of the forties, new particles were discovered, including the K^+ meson [2] (then variously denoted τ, κ, or χ, depending on its decay), and the Λ [3] (then denoted V^0_S). These hadrons and other weakly decaying baryons were termed 'strange' due to their long lifetimes ($\sim 10^{-10}$s). Collectively, the strange baryons were termed 'hyperons'. Hypercharge, or more fundamentally, the strangeness quantum number S, conserved by

the strong nuclear force, but not the weak, was introduced by Gell-Mann [4] and, independently, Nakayo and Nishijima [5, 6]).

Descriptions of baryons by constituent quarks have been developed, so that protons and neutrons are envisioned as collections of up and down quarks (uud and udd, respectively). Hyperons implied a third quark, the S=-1 strange quark (denoted s). The quark content of hyperons was then surmised; Λ (uds), Σ (uus, uds, dds), Ξ (uss, dss), and Ω (sss). Considerations of the strangeness degree of freedom led to the prediction of the Ω^- by both Gell-Mann and (independently) Ne'eman [7], which was discovered at Brookhaven in 1964 [8].

Despite our familiarity with hyperons, strangeness remains relatively unexplored theoretically, a fact due predominantly to the difficulty in producing nuclei containing strange baryons [9]. Hypernuclei with S=-1, i.e. nuclei containing a singly-strange hyperon such as a Λ (or possibly a Σ), have been studied, and excellent reviews exist [10, 11, 12]. These experiments made use of the strangeness exchange reaction (K^-, π^-), and to a lesser extent, associated production in the form of (π^+, K^+) or (γ, K). The (K^-, π^-) reaction has the advantage that the momentum transfer q is limited, and there exists a 'magic' momentum p_K at which q indeed vanishes at 0° [10]. Associated production (π^+, K^+) has greater momentum transfer, but tends to preferentially populate high spin states, so that the two hypernuclear production reactions complement each other.

Highlights of research in the S=-1 sector are multifold. Roughly thirty-three isotopes of single-Λ hypernuclei have been observed, in sixteen different elements [13]. Binding energies of the Λ range from a tenth of an MeV up to approximately 24 MeV. The Λ potential well depth has been shown to be $\approx$ 30 MeV deep. Hypernuclear gamma rays have been detected, identifying radiative transitions between hypernuclear levels. This is particularly important in the investigation of the Λ-nuclear interaction. The splitting of Λ spin multiplets is too small to be measured in magnetic spectrometers [10].

However, almost no data exist for hypernuclei with strangeness S≤ -2. A natural extension to the above mentioned strange baryon-producing reactions is the double-charge exchange, double-strangeness exchange reaction (K^-, K^+) , employed by experiment 885.

More generally, the question of what form matter takes when two or more strange quarks are present remains unanswered. Strange quarks may be bound in hyperons in a conventional nuclear physics picture. Or, they may mix freely in a state known as strange quark matter (SQM), first postulated in 1971 [14]: confined objects containing a large number of delocalized up, down and strange quarks [9]. Predictions for these forms of 3-flavour matter are based on the Pauli exclusion principle, symmetry considerations, and the nature of the colour-magnetic interaction of the quarks. E885 is a high statistics experiment intended to provide insight into the nature of matter when precisely these conditions are met - when several strange quarks are added to the nuclear medium. The experiment includes searches for $\Lambda\Lambda$-hypernuclei, Ξ-hypernuclei, and the H-dibaryon [15]. The latter, having the quark-content of two Λ's ($uuddss$), is an example of strange quark matter, the lightest "strangelet" thought to exist. Two Λ's in a nucleus would fuse to form a deeply bound H if such a configuration were energetically favourable. In turn, the existence of the H, even as an unbound resonance, will impact the possible nature of $\Lambda\Lambda$ and Ξ-hypernuclei [16].

1.2 Physics motivations

It is highly desirable to obtain a global characterization of the baryon-baryon (BB) interaction. Relatively well parametrized, via potential models, are conventional nucleon-nucleon (NN) interactions. Scattering data and bound states are well reproduced. Extensions into the strangeness sector are often in the form of one-boson exchange (OBE) models, for example, the Nijmegen group's attempt to

simultaneously describe data on BB systems by extending their models into the hyperon-nucleon (YN) arena [17, 18]. However, there is such a paucity of hyperon-hyperon (YY) data that many OBE models still compete. Despite over thirty years passing since the discovery of the first $\Lambda\Lambda$-hypernucleus candidate, it is still unclear whether the $\Lambda\Lambda$ interaction is repulsive or attractive [19].

The H-dibaryon would be the lightest strangelet, an example of strange quark matter (SQM). The observation of the H would indicate that in at least some cases, the degrees of freedom that best describe the strange nuclear medium are quark ones, rather than baryonic.

If Ξ-hypernuclei indeed prove bound, but if at the same time the Ξ well depth is too shallow, strange hadronic matter (SHM) may be unable to form [16, 20]. SHM is a hypothetical form of matter, stable against strong decay, composed of protons, neutrons, Λ's and Ξ's. In these systems, filled Λ orbitals preclude the strong decay

$$\Xi N \rightarrow \Lambda\Lambda \tag{1.1}$$

via Pauli blocking. Because of binding effects, the reverse reaction ($\Lambda\Lambda \rightarrow \Xi N$) is also accessible in heavier multi-Λ hypernuclei, and SHM necessarily includes both Λ and Ξ hyperons, so that eq. 1.1 can ultimately be Pauli blocked in both directions. Characteristics of SHM include a large strangeness fraction $\mid S \mid /A \approx 1$, a small charge fraction $-0.1 < q/A < 0.1$, and a density two to three times that of ordinary nuclear matter [21]. Thus SHM is very similar to SQM, with the exception that the former has a lower binding energy per particle $E_B/A \approx -10$ to - 20 MeV (ibid). Now if the Ξ well depth $V_{0\Xi}$ is as shallow as some 10-15 MeV, the strong conversion $\Lambda\Lambda \rightarrow \Xi N$ will not take place, hence not enough Ξ's will be present for SHM to form [22]. The Ξ hyperons would bring substantial strangeness, and Ξ^- baryons counter the proton Coulomb repulsion, both integral points for the formation of SHM.

1.3 Previous experimental results in the S=-2 sector

Data in the S=-2 sector are extremely limited. This is due to several effects, including low production cross-sections and high momentum transfers of the reactions involved. Further hampering some production modes, such as for double Λ-hypernuclei, is the two step nature of the reaction process. To date there exist only a handful of candidates for S=-2 exotic objects. We concentrate here on Ξ-hypernuclei, but briefly consider other S=-2 candidates.

1.3.1 ΛΛ-hypernuclei

The three examples of ΛΛ-hypernuclei all come from studies of stopped Ξ^- in emulsion [23, 24, 25]. Emulsion film, composed of light (H, C, N, O) and heavy (Br, Ag) nuclei, is irradiated with a K^- beam and later inspected. The goal is to reconstruct the event, identify the charge of the nuclear core and the binding energy of the attached hyperon.

Table 1.1 summarizes the three reported ΛΛ-hypernuclei. It is interesting to note that while only one or two Ξ hyperons stopped in the emulsion from the first experiment, no other likely interpretation has been found for the decay topology. Emulsion plates from the second experiment were lost, and hence have never been scrutinized as thoroughly as those of the first. The two references ([25, 26]) for the third event from KEK-E176, refer to the two existing interpretations of the event, yielding disparate predictions for the ΛΛ interaction. While a consistent interpretation of the three emulsion events is available, indicating a strongly attractive residual ΛΛ interaction of about 5 MeV, a repulsive one cannot yet be ruled out. The interpretation of the most recent event, favoured by Dover *et al.* [26] and restoring a positive ΛΛ interaction, requires a decay topology that has very limited phase space [19].

Candidate hypernucleus	K^-	Ξ^- stops	$\Delta B_{\Lambda\Lambda}$ (MeV)	collaboration, year, reference
${}^{10}_{\Lambda\Lambda}$Be	10^5	~ 2	4.3 ± 0.4	Danyz *et al.*, 1963 [23]
${}^{6}_{\Lambda\Lambda}$He	10^5	~ 30	4.7 ± 1.0	Prowse, 1965 [24]
${}^{10}_{\Lambda\Lambda}$Be	10^5	80	-4.9 ± 0.7	Aoki *et al.*, 1991 [25]
or				
${}^{14}_{\Lambda\Lambda}$C*			4.8 ± 0.7	Dover *et al.*, 1991 [26]

Table 1.1: Candidate $\Lambda\Lambda$-hypernuclear events. All events were produced by Ξ^- baryons stopping in emulsion. The $\Lambda\Lambda$ binding energy, $\Delta B_{\Lambda\Lambda} = B_{\Lambda\Lambda} - 2B_{\Lambda}$, represents the modification to the binding energy of the two Λ's due to the $\Lambda\Lambda$ interaction.

1.3.2 The H-dibaryon

It is interesting to note that the H-dibaryon is not an artifact of the bag model, and appears inherent to QCD. Many models (e.g. bag models, non-relativistic and relativistic potential models, Skyrme models, Lattice QCD approaches, etc.) predict a six-quark state stable against strong decay. However, no experiment to date has been able to unambiguously establish the existence of the H-dibaryon. R. W. Stotzer [27] includes a particularly complete compilation of theoretical and experimental references pertaining to the H. Furthermore, experiments have been able to convincingly demonstrate that a deeply bound H (a mass range extending some 50 MeV/c^2 to 380 MeV/c^2 below the $\Lambda\Lambda$ -threshold) is exceedingly unlikely [28].

The $\Lambda\Lambda$-hypernuclei candidates of Table 1.1 also constrain the H mass. A pair of Λ's bound in a nucleus will decay strongly to an H-dibaryon if $M_H < 2M_\Lambda - B_{\Lambda\Lambda}$. The third of the three $\Lambda\Lambda$ candidates sets mass limits of M_H >2.2228 GeV/c^2 [25] and M_H >2.204 GeV/c^2 [25, 26] for the two interpretations of the event.

Analysis of $\Lambda\Lambda$-hypernuclei candidates, plus the findings of BNL-E836 [27, 28] suggest that if the H-dibaryon exists, it must be either loosely bound or an unbound resonance. Some suggestion of an unbound resonance is found in the analysis of KEK-E224 scintillating fibre images. Ahn *et al.* [29] interpret an enhancement of production of $\Lambda\Lambda$ pairs near threshold (2.23 GeV/c^2) as indication of the formation of an H-dibaryon resonance state. Whether or not the enhancement corresponds to a resonance state remains unclear; Ohnishi *et al.* [30] have successfully modelled the KEK-E224 result using an attractive final state interaction. Results of the BNL-E813 search for a loosely bound H-dibaryon are expected to be published in the near future [31].

1.3.3 Ξ-hypernuclei

Emulsion events

Seven emulsion events have been reconstructed and attributed to the formation of Ξ-hypernuclear states, where the Ξ baryon is interpreted to have been bound via the strong nuclear force within the nucleus. Table 1.2 summarizes these events. In other emulsion events (see, for example, [32]), the Ξ^- is determined to have been captured on a nucleus, yet neither can the binding energy be calculated nor can the identity of the nuclear core to which it is attached be established.

All events summarized in Table 1.2 were obtained by irradiating emulsion film[1] with K^-'s of 3.0-10.0 GeV/c. In each case, a study of the emulsion revealed the emission of two hyperfragments from the interaction point of the K^- meson with an emulsion nucleus. However, this scenario does not kinematically constrain the event to the formation of nuclear bound states of the Ξ. Furthermore, it is possible that neutral particles were missed in the analysis of the emulsion events, which would lead to an estimate of a deeper Ξ binding energy than reality.

[1] Illford K5 or G5 nuclear emulsion film.

Two more recent events [33] come from the hybrid emulsion-spectrometer experiment KEK-E176 (the same experiment that produced the third of the three $\Lambda\Lambda$ events). These candidate events are superior to those of Table 1.2 because the Ξ^- is identified and then captured at rest. However, multiple interpretations for these events remain.

Candidate hypernucleus	B_Ξ (MeV)	laboratory, year, reference
${}^{8}_{\Xi}$He	5.9 ± 1.2	Berkeley, 1959 [34]
${}^{11}_{\Xi}$B	9.2 ± 2.2	CERN, 1969 [35]
${}^{13}_{\Xi}$C	18.1 ± 3.2	CERN, 1979 [36]
${}^{15}_{\Xi}$C	16.0 ± 4.7	CERN, 1967 [37]
${}^{17}_{\Xi}$O	16.0 ± 5.5	CERN, 1967 [37]
${}^{28}_{\Xi}$Al	23.2 ± 6.8	CERN, 1967 [37]
${}^{29,30}_{\Xi}$Mg	2.4 ± 6.3	CERN, 1967 [37]

Table 1.2: Emulsion events, candidates for Ξ-hypernuclei. These data were used in an analysis by Dover and Gal [1] to obtain estimates of the Ξ nucleus potential $V_{0\Xi}$.

Spectrometer measurement

Emulsion studies are limited in that they obtain ground state binding energies of light (A<16) hypernuclei. With the advent of intense K^- beams and magnetic spectrometers, the general spectroscopy of hypernuclear states becomes available for study.

KEK-E224 was a spectrometer-based experiment that, like E885, made use of scintillating fibre detectors, or SCIFI (see Section 2.4.1). E224 used the SCIFI as an active target, instead of an out-of-beam detector as did E885. A search was carried out for doubly-strange hypernuclei using the (K^-, K^+) reaction on

carbon in the scintillating fibres:

$$K^- + {}^{12}C \rightarrow {}^{12}_{\Xi} Be + K^+. \tag{1.2}$$

Results from the spectrometer measurement of E224 have recently been published [38]. Despite low statistics, they find an excess of events below the quasi-free Ξ^- production peak, consistent with Ξ-hypernuclear production. Finding three events in the bound region, they extract a Woods-Saxon Ξ well depth of $V_{0\Xi} = 16 - 17$MeV.

This well depth is consistent with the KEK-E176 twin hypernuclear production event, analyzed by Yamamoto *et al.* [39] to give $V_{0\Xi} \approx 16$MeV. Note that this result is considerably more shallow than the $V_{0\Xi}$ =21-24MeV derived from analysis of the older emulsion data. Fitting the tail of the spectrum of quasi-free production of Ξ^-, as performed for KEK-E224 and in this thesis for E885, however, is expected to be model-dependent, and both the well-depth and width may be adjusted as free parameters [40]. This effect is investigated in the analysis of the excitation spectrum in Section 4.6.4, in which various theoretical curves for different well-depths $V_{0\Xi}$ will be compared to E885 data.

In short, very little definite information has been obtained in the S=-2 sector. A high statistics experiment is required to settle the questions surrounding the form matter takes when containing several strange quarks.

1.4 Ξ-hypernuclei: directions from theory

Dover and Gal [1] reviewed the available emulsion candidates for Ξ-hypernuclei, in order to extract the well depth of the Ξ-nucleus potential. Table 1.2 summarizes the candidate Ξ-hypernuclei observed, and respective binding energies B_{Ξ} as deduced by the experimenters. Dover and Gal then fit these data to a

phenomenological Woods-Saxon potential of the form

$$V_{\Xi} = -V_{0\Xi}(1 + e^{(r-R)/a})^{-1}. \tag{1.3}$$

Here $V_{0\Xi}$ is the depth parameter, R=r_0A$^{1/3}$, and a = 0.65 fm is the surface diffuseness. Their method is to assume a reasonable value for the radius parameter r_0, and then adjust the V_{Ξ} for each nuclear species to reproduce the observed B_{Ξ}. For two different selections of r_0, Dover and Gal find best fit values of

$$V_{0\Xi} = 24 \pm 4 \quad \text{MeV for } r_0 = 1.1 \text{ fm},$$
$$V_{0\Xi} = 21 \pm 4 \quad \text{MeV for } r_0 = 1.25 \text{ fm}.$$

for the Ξ-nucleus well depth.

Dover and Gal note that none of the interpretations of the emulsion data are statistically unique, and some are hardly compelling. All of the candidate events consist of emulsion tracks in which an incident particle, presumed to be a K^- (or possibly a π^-), interacts with an emulsion nucleus, producing a decay star. Two tracks in each decay star are identified as hyperfragments, postulated to be due to the decay of the Ξ-hypernucleus, which is expected to strongly convert via $\Xi N \rightarrow \Lambda\Lambda$ in $\sim 10^{-20}$ s. As the lifetime of the Ξ-hypernucleus is so short, its recoil does not leave any track in the emulsion. However, this scenario, in which two hyperfragments are emitted from a mesonic interaction point, does not kinematically ensure formation of nuclear bound states of the Ξ^-. Furthermore, as neutral particles leave no tracks in the emulsion, energy may have been taken away in the form of kinetic energy of missed particles, leading to an estimate of $V_{0\Xi}$ that is deeper than reality.

Calculations of the (K^-, K^+) cross sections for Ξ hypernuclear states within the framework of the distorted-wave impulse approximation (DWIA) have been performed [1, 41, 42]. The DWIA has successfully been used to predict cross-sections for S=-1 Λ hypernuclear production using in-flight (K^-, π^-) and (π^+, K^+)

reactions. A natural extension of this process is to apply the framework to the (K^-, K^+) reaction. Forward nuclear cross sections ($\theta = 0°$) were found to be at the level of a few tens of nb/sr to 1 μb/sr, for $p_{lab} = 1.9$ GeV/c (ibid). This corresponds to the probability of producing a cascade directly in a nuclear bound state to be about 1 percent of the total Ξ^- produced in (K^-, K^+) reactions. Thus ("quasi-discrete") bound Ξ hypernuclear states are expected to be accessible via the (K^-, K^+) reaction, and be sufficiently separated from the quasi-free Ξ production region, which has an integrated cross-section 2 orders of magnitude greater than that of the hypernuclear production.

Both the 1s and 1p-orbitals are expected to be bound for $V_{0\Xi} \geq 20$ MeV [1, 41, 42], whereas only the 1s is expected to be bound for $V_{0\Xi}$ =16MeV (ibid). Examining the conversion mechanism $\Xi N \rightarrow \Lambda\Lambda$, these same authors arrive at somewhat different expectations for the width of the Ξ states. Dover and Gal [1] first obtained widths of $\Gamma \leq 5 - 10$ MeV, while more recent calculations favour narrower states of $\Gamma \leq 2$ MeV [41, 42, 43]. A one-boson exchange (OBE) model is used to estimate the $\Xi N \rightarrow \Lambda\Lambda$ conversion rate .

Other theoretical estimates for $V_{0\Xi}$ have been made. A relativistic mean field calculation performed by Schaffner *et al.* [21] produced a deeper Ξ well depth of $V_{0\Xi} = 28$ MeV. Using the OBE model D of the Nijmegen group [44, 17], Dover and Gal [45] obtain a $V_{0\Xi}$ very close to that of their emulsion analysis.

The search for Ξ-hypernuclei in E885 derives some motivation from the S=-1 sector. In particular, the unexpected observation of *relatively* narrow Σ-hypernuclear states[2] would seem to imply the existence of Ξ-hypernuclei [1]. Several arguments are advanced as to why Ξ-hypernuclei, which would decay strongly via $\Xi N \rightarrow \Lambda\Lambda$ conversion, should have smaller conversion widths than their Σ counterparts. For example, far less phase space is available for the $\Xi N \rightarrow \Lambda\Lambda$ strong conversion

[2]Here, "relatively narrow" refers to widths of a few MeV, as opposed to "too broad to obtain spectroscopic information".

($Q \sim 25$ MeV) than for $\Sigma N \rightarrow \Lambda N$ ($Q \sim 80$ MeV). Furthermore, because of the Pauli exclusion principle for the two Λ's, the initial ΞN system is constrained to quantum numbers of $^1S_0$, I=0 [10]. It is interesting to note that recently, narrow ${}^{4}_{\Sigma}He$ states, roughly 7 MeV wide, have been observed [46]. No other bound Σ-hypernuclei have been unequivocably observed.

1.5 BNL-AGS experiment 885

Experiment 885 was performed on the D6 beamline of the Alternating Gradient Synchrotron, at Brookhaven National Laboratory. The beamline [47] was created for the related H-dibaryon searches E813/836, which ran in 1992-1995. Experiment 885 was run in production mode for four months of the 1996 Slow Extracted Beam, or SEB period.

The experiment was originally conceived [48] as a measurement of the ground state of ${}^{6}_{\Lambda\Lambda}$He using stopped Ξ^-'s:

$$(\Xi^-, {}^{6}Li)_{atom} \rightarrow {}^{6}_{\Lambda\Lambda}He + \mathrm{n}. \tag{1.4}$$

The branching fraction for the above reaction has been calculated by Zhu *et al.* [49]; approximately 5% of Ξ^- stops should yield a ${}^{6}_{\Lambda\Lambda}$He. While this should produce a large yield of monoenergetic neutrons to indicate the formation of double-Λ hypernuclei, concerns about the neutron background suggested that the signal-noise would be marginal [19]. This led to the use of a ^{12}C scintillating fibre option, first as an active target, and then finally as an out-of-beam decay particle detector, with a 660 carat industrial diamond (carbon) as the target.

E885 used the double-charge exchange, double-strangeness exchange (K^-, K^+) reaction to produce Ξ^- baryons and investigate doubly-strange species. Typically, in a quasi-free process, the incident K^- produced a Ξ^- by interacting with a proton

bound in a carbon nucleus:

$$K^- + {}^{12}C \rightarrow \Xi^- + K^+ + X, \tag{1.5}$$

Primary goals of the experiment were to: i) search for $\Lambda\Lambda$-hypernuclei produced by stopping Ξ^- hyperons in carbon:

$$(\Xi^-, {}^{12}C)_{atom} \rightarrow {}^{12}_{\Lambda\Lambda}B + \mathrm{n}, \tag{1.6}$$

ii) directly produce Ξ and $\Lambda\Lambda$-hypernuclei via

$$K^- + {}^{12}C \rightarrow {}^{12}_{\Xi}Be + K^+, \tag{1.7}$$

$$K^- + {}^{12}C \rightarrow {}^{12}_{\Lambda\Lambda}Be + K^+, \tag{1.8}$$

and iii) search for H-dibaryons produced both directly and with stopped Ξ^-:

$$K^- + {}^{12}C \rightarrow H + K^+ + X, \tag{1.9}$$

$$(\Xi^-, {}^{12}C)_{atom} \rightarrow H + {}^{11}B. \tag{1.10}$$

This thesis reports on a spectrometer-based search for ${}^{12}_{\Xi}Be$, using the channel given in Equation 1.7.

S=-2 hypernuclei from the direct production on carbon may be distinguished in two ways. Ξ and $\Lambda\Lambda$-hypernuclear states are expected to be well separated in excitation energy (the Q value for Ξp$\rightarrow \Lambda\Lambda$ is 28.2 MeV), much like the case of the S=-1 Λ and Σ hypernuclei [1]. Furthermore, Ξ-hypernuclei are expected to decay via

$${}^{12}_{\Xi}Be \rightarrow {}^{11}_{\Lambda\Lambda}Be + \mathrm{n}$$

with a branching ratio of $\sim$ 20% [43]. Neutron detectors are employed in E885 which may detect the monoenergetic signal from the decay of ${}^{12}_{\Xi}Be$ hypernuclei.

While the D6-line spectrometer has modest resolution ($\sigma = 4.1$ MeV/c^2 r.m.s. for hydrogen kinematics) so that it will not be possible to resolve individual hypernuclear states, cross section limits will be set.

In the the next two chapters we describe the experimental apparatus. The first of the two experimental chapters gives an overview of hardware such as the beamline, spectrometer, targets and triggers, while the latter chapter details the gas-microstrip vertex detectors. Chapter 4 explains the data analysis. The remainder of the thesis is devoted to results and discussion.

Chapter 2

Experimental Setup

We divide the experimental apparatus up into the following sections: i) the kaon beamline including the mass slit area, and the incident beam detectors upstream of the target, ii) the spectrometer, including the forward region (between the carbon target and the 48D48 spectrometer magnet), the magnet itself, and the back region (consisting of detector elements downstream of the 48D48), and iii) the out-of-beam detectors, iv) the target, and v) triggers.

2.1 Conventions

2.1.1 Detector naming conventions

A schematic diagram of the E885 beamline and apparatus is given in Fig. 2.1. The beamline and apparatus are divided into logical regions, both for nomenclature purposes, and for breaking down analysis tasks into simpler units. The regions are labelled as follows:

M : mass slit area

I : incident area

L : beam left

R : beam right

F : front area

B : back area

Here, "beam left" refers to the "left of the beamline", when looking in the direction of travel of the K^- beam, and conversely, for "beam right".

Several basic detector types are used in the experiment; each type of detector has its own label:

P : position-sensitive scintillator hodoscope

T : timing scintillator

D : drift chamber

C : Čerenkov detector

M : microstrip gas chamber

V : charged particle veto detector (scintillator)

A given detector has a label that consists of two letters and a number. The first letter gives the region in which it resides, the second, the type of detector it is, and the number enumerates detectors of that type in the region. For example, FM2 denotes the second microstrip gas chamber in the forward region. The scintillating fibre detectors and neutron detectors (left and right) did not conform to these naming conventions, and were instead denoted SCIFI, LN and RN, respectively.

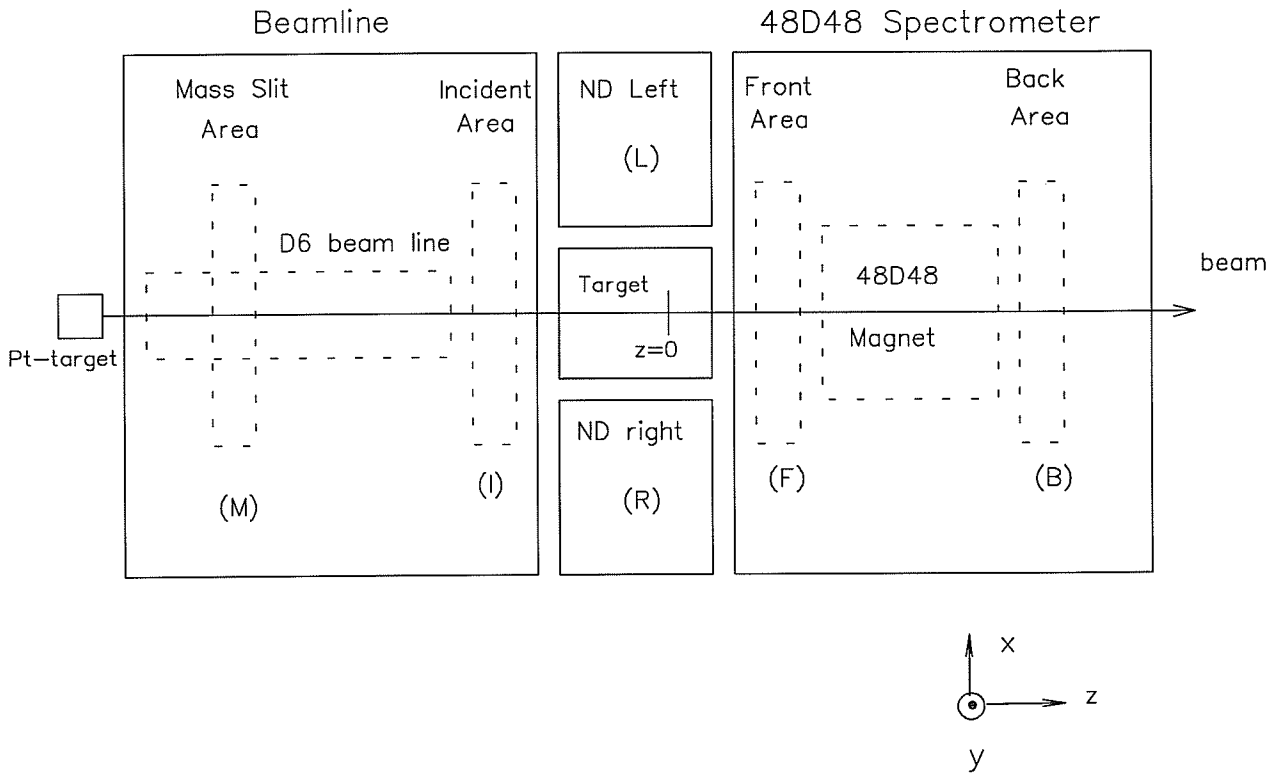

Figure 2.1: Schematic diagram of experimental setup.

2.1.2 Coordinate systems

The primary coordinate system used in the experiment is a right-handed cartesian one, with an origin 2.00 m upstream of the center of the 48D48 magnetic field. The z axis runs parallel to the beam, increasing along the direction of particle travel. The y axis increases vertically, and the x axis is thus selected in order for the coordinate system to be right-handed: looking downstream, the x axis increases to the left. Angles θ and ϕ are defined relative to the primary coordinate system in Fig. 2.2.

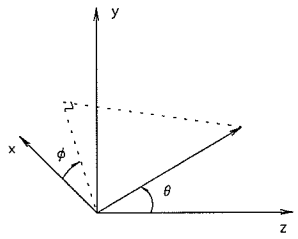

Figure 2.2: Directional angles θ and ϕ in E885.

2.2 The D6 beamline

2.2.1 Beamline and mass slit region

The D6 beamline (Fig. 2.3) at the AGS is the world's most intense source of separated kaons. The beamline was constructed for the related H-dibaryon searches E813/836 [50, 27], and is described in more detail elsewhere [47]. Protons of energy 24 GeV/c are incident on a platinum production target, sending a variety of secondary particles into the D6 beamline. Two stages of electrostatic separation and magnetic velocity filtering are performed to select K^- mesons, and reduce background contamination in the form of pions, muons, electrons and antiprotons. The electrostatic separators each held 600 kV across a 10.0 cm gap; 80%

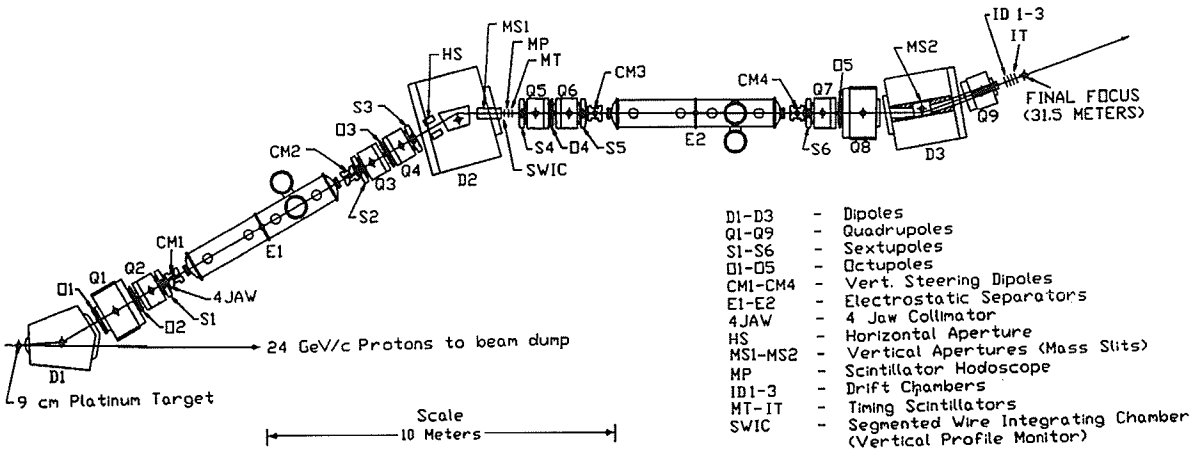

Figure 2.3: Plan view of the BNL-AGS D6 beamline.

of their design voltage. Typical AGS intensities afforded to D6-line in 1996 were 5×10^{12} protons per spill incident on the primary target, with a spill duration of 1.6 s and a repetition rate of 1000 spills/hour (44% duty factor). This resulted in a secondary K^- flux in the D6 beamline of approximately 10^6/spill, with an excellent K^-/π^- ratio of approximately unity.

While the momentum of the beam particles can be selected from 1-2 GeV/c, a nominal value of 1.8 GeV/c was chosen, as the cross-section for the production of discrete Ξ hypernuclear states is expected to peak here [1]. The momentum spread of the beam is roughly 150 MeV/c.

MP

A measurement of beam particle momenta was made with hits in a scintillating hodoscope detector MP (along with position measurements via downstream drift chambers ID1-3 and microstrip chamber IM1). Some characteristics of MP are given in Table 2.1, which includes important parameters of all hodoscopes used in the experiment. The detector consisted of 72 scintillator elements staggered along

the x-axis, in order ensure complete coverage of the acceptance. Each scintillator element was coupled to a single R647-01 photomultiplier tube (PMT). MP was located downstream of dipole magnet D2 and the first mass slit MS1, with the center of the scintillator detector situated at x = 0.0 mm, y = 0.0 mm, z = -4.400 m.

MT

Timing of the beam particle is given by MT, situated just downstream of MP. MT was composed of 9 elements arranged along the x axis. MT characteristics are shown in Table 2.1. Each scintillator bar was viewed by two RCA8575 PMT's. The timing hodoscope was placed downstream of MP, centered at x = 0.0 mm, y = 0.0 mm, z = -4.300 m.

Detector	Number of elements	Segmentation	Active area (mm^2)	Dimensions(mm)			Inclination to y axis
				x	y	z	
MP	72	x	330.0 × 15.0	7.0	15.0	3.18	0°
MT	9	x	4950.0	37.0	15.0	6.35	0°
IT	4	x	3000.0	25.0	30.0	12.7	0°
FP	16	y	57600.0	240.0	15.0	4.0	0°
BP	6	x	2268000.0	210.0	1800.0	12.7	30°
BT	40	y	6600000.0	2000.0	85.0	50.0	15°

Table 2.1: Specifications of the scintillator hodoscope detectors used in the E885 spectrometer. The dimensions given in the fifth column correspond to the extents of a single element of the hodoscope.

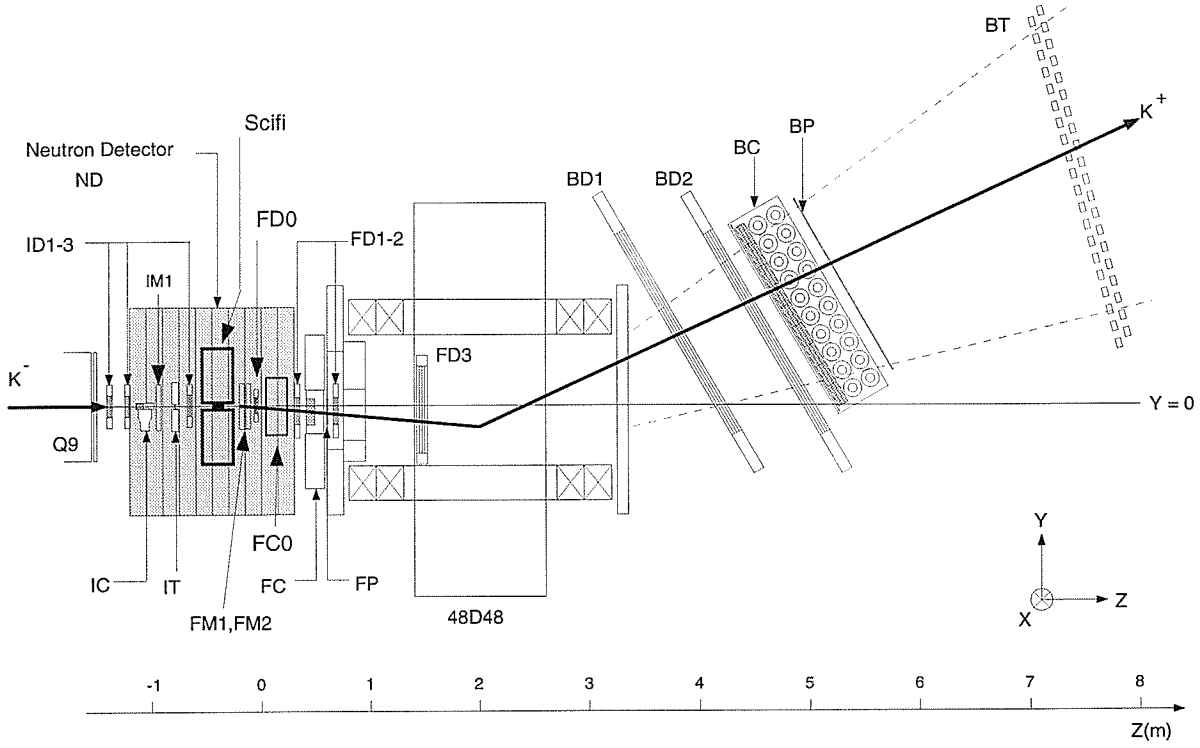

Figure 2.4: Side view of the E885 spectrometer and associated detectors.

2.2.2 Incident area

Downstream of the final beamline quadrupole, Q09, is the E885 experimental apparatus. Fig. 2.4 is a side-view of the target, spectrometer, and associated detectors.

Čerenkov detector IC

Čerenkov detectors exploit the phenomenon whereby charged particles, when traversing a dielectric medium with a velocity exceeding that of light in the material, will radiate in the visible spectrum. The threshold for the production of

Čerenkov radiation is given by $\beta_t = 1/n$, where n is the index of refraction of the radiator. For a given momentum, particles of different mass have different velocities, so that an appropriately selected material will cause one species of particle to emit Čerenkov radiation, while the other will not. Particle identification (PID) is accomplished observing whether or not Čerenkov radiation is produced in a detector. In E885, K^-/π^-, K^+/p and K^+/π^+ separation is achieved via carefully selected radiators for Čerenkov detectors. Table 2.2 lists some of the characteristics of the detectors used in the experiment.

Detector	Purpose	Number of radiators	Total active area (mm^2)	Dimensions(mm)			Index of refraction
				x	y	z	
IC	π^-/K^- sep.	2	100.0×50.0	100.0	50.0	30.0	1.029
FC0	K^+/proton sep.	8	130.0×140.0	130.0	18.0	36.0	1.107-1.136
FC	π^+/K^+ sep.	16	230.0×230.0	115.0	115.0	20.0	1.037
BC	π^+/K^+ sep.	162	1260.0×1890.0	210.0	210.0	30.0	1.04

Table 2.2: Specifications of the Čerenkov detectors used in the E885 spectrometer. The dimensions given in the fifth column correspond to individual block (radiator) extents.

Upstream of the target, the detector IC, situated between ID2 and IM1, distinguishes between kaons and pions. The detector employs a radiator consisting of 2 pieces of silica aerogel with index of refraction n=1.029. This corresponds to a β_t of 0.972. Light from the aerogel block is imaged by a single 12.7cm Hamamatsu R1250 PMT. Given pions of 1.8 GeV/c have $\beta_\pi = 0.997$, and kaons of 1.8 GeV/c have $\beta_K = 0.964$, the former will fire IC, while the latter will not. Hardware triggers incorporate the discriminated signal of IC to veto pions. Potential ${}^{12}_{\Xi}$Be events (the so-called "KK" events, or ones with a primary K^- and a secondary K^+) trigger the data acquisition system only when IC does not fire, indicating the beam particle was not a pion. Using a second Čerenkov detector, identical to

IC, the efficiency for detecting 1.8 GeV/c π's was found to be 99.7% [50].

Timing hodoscope IT

The time reference for all time-of-flight (TOF) measurements is given by hits in the scintillator hodoscope IT. Located at $x = 0.0$ mm, $y = 0.0$ mm, and $z = -560.3$ mm, the detector consists of four vertically-arranged BC408 scintillators, viewed on either end by RCA8575 photomultiplier tubes (PMT). IT was measured, using constant fraction discriminators, to have an intrinsic time resolution of $\sigma = 130$ ps. Please see Table 2.1 for details of the IT timing hodoscope.

Drift chambers ID1-3

Drift chambers ID1-3 tracked beam particles emerging from the last beamline quadrupole Q09, to the target, situated near the beam waist at z=-200.0 mm. An active area of 2311.5 mm^2 was formed by three double-planes oriented to measure in x, u and v directions. Parameters of the identical detectors are given in Table 2.3. Note that ID wire planes were arranged to give the best measurement resolution in the x direction, critical for evaluating the momentum of the beam particle. Each double plane consists of 48 wires, half of which are offset by 2.54 mm to resolve hit ambiguities. The double-plane configuration used in many of the E885 drift chambers is useful in rejecting accidentals, a common occurrence in high-rate environments. The fill gas used in the ID chambers was a so-called magic gas mixture: 76% argon, 20% isobutane for quenching photons, and 4% methylal, a nonpolymerizing agent that acted as a cleaning agent.

Microstrip gas chambers IM1, FM1-2

Microstrip gas chambers (MSGC) are a relatively new type of gaseous position-sensitive detector [51]. The University of Manitoba/TRIUMF group constructed

and tested four MSGCs to act as a vertex detector in the experiment. Three chambers were installed in the beamline; IM1 upstream, and FM1-2 downstream of the target. Parameters of the microstrip chambers are given in Table 2.4.

As the MSGC constituted the major hardware contribution of this thesis project, the next chapter is devoted to a description of MSGC design, testing and operation.

Chamber	Planes	Rotation angle	Spacing (mm)	Location(mm)			Resolution (mm)	Channels
				x	y	z		
ID1	$u-u$'	120°	5.08	0.0	0.18	-1342.4	0.15	24×2
	$v-v$'	60°	5.08				0.15	24×2
	$x-x$'	0°	5.08				0.15	24×2
ID2	$u-u$'	120°	5.08	-0.07	1.27	-1178.7	0.15	24×2
	$v-v$'	60°	5.08				0.15	24×2
	$x-x$'	0°	5.08				0.15	24×2
ID3	$u-u$'	120°	5.08	-0.65	0.90	-416.7	0.15	24×2
	$v-v$'	60°	5.08				0.15	24×2
	$x-x$'	0°	5.08				0.15	24×2

Table 2.3: Specifications of the ID chambers. The definition of the rotation angles is shown in Fig. 2.5. 'Spacing' denotes the chamber sense wire spacing, 'Location' refers to the position of the center of the chamber, and 'Resolution' is the position measurement resolution.

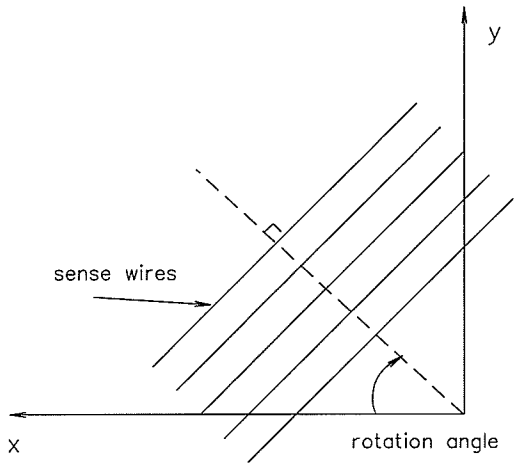

Figure 2.5: Wire orientation and rotational angle definition in E885 drift chambers.

MSGC	Planes	Rotation angle	Pitch (mm)	Location(mm)			Resolution (mm)	Channels
				x	y	z		
	x	0°	1.00				0.50	80
IM1	y	90°	0.50	0.0	-0.7	-1351.9	0.25	96
	x	0°	1.00				0.50	80
FM1	y	90°	0.50	5.0	-3.4	-91.6	0.25	96
	x	0°	1.00				0.50	80
FM2	y	90°	0.50	1.5	-0.5	-879.5	0.25	96

Table 2.4: Specifications of the microstrip chambers. The definition of the rotation angles is shown in Fig. 2.5. Here, 'Spacing' denotes the anode pitch of the microstrip print, 'Location' refers to the position of the center of the chamber, and 'Resolution' is one-half of the strip pitch.

2.3 E885 spectrometer

2.3.1 Forward region

The region between the diamond target and the 48D48 dipole bending magnet is termed "forward". Detectors in the forward region are intended to analyze the scattered, or secondary particles, and separate them from non-interacting beam particles. Residual beam traverses the target, multiple scatters, and then is directed by the 48D48 into the floor in the back region. Forward detectors shown in Fig. 2.4 include microstrip gas chambers FM1-2, drift chambers FD0-3, Čerenkov detectors FC0 and FC, and scintillator hodoscope FP.

Čerenkov detectors FC0 and FC

While Čerenkov detectors IC, FC and BC are designed to distinguish between kaons and pions, FC0 was intended to separate protons and K^+s (see Table 2.2). The detector was located downstream of FD0, and just upstream of FC. Fabricated specially for the H-dibaryon search E836, the index of refraction of the silica aerogel radiator of FC0 varied from n=1.136 (top) to 1.107 (bottom). Previously, only liquid H_2 could achieve a comparable index. Given that the primary source of background in the back region of the spectrometer consists of protons scattered elastically and inelastically from the target, FC0 was designed to radiate for kaons above a momentum threshold, but not for the majority of protons, below threshold. For example, the average index of refraction of FC0 is approximately 1.12, corresponding to a threshold of $\beta_t = 0.89$, or respective kaon and proton momentum thresholds of $p_{K^+} > 0.98$ GeV/c and $p_p > 1.86$ GeV/c.

As light output from a Čerenkov radiator increases with index of refraction n, and most scattered K^+'s exit the target at small forward angles, the bars are arranged in descending index of refraction, as noted above. The eight aerogel radiators were viewed by eight 50.8 mm Hamamatsu H1161Q PMTs. Details of

the FC0 detector can be found in [27].

Despite the addition of a specialized Čerenkov detector in the forward region to suppress proton background, a second level trigger was necessary. A minor inefficiency in FC0 could potentially overwhelm the trigger rate of the experiment with unwanted (K^-, p) scatter. Section 2.6.2 gives some details of the second level trigger.

Čerenkov detector FC (upgraded from that used in experiments 813 and 836) separated scattered K^+ from π^+ in the forward region of the spectrometer. Consisting of 16 bars of silica aerogel with an index of refraction of $n = 1.037$, the detector was located downstream of FC0, and just prior to hodoscope FP. Table 2.2 gives more parameters of the detector. K^+s had a threshold momentum of 1.729 GeV/c, while π^+s had a threshold of 0.49 GeV/c in the detector. FC is used in the hardware trigger to ensure pions are not mistaken for kaons in the forward region of the spectrometer.

Scintillator hodoscope FP

A critical detector for trigger formation is the scintillator hodoscope FP, its center located downstream of the target at x = 0.0 mm, y = -68.0 mm, z = 600.0 mm. The detector consists of 16 slats of BC408 scintillator segmented in the y-direction, each slat viewed from either end by Hamamatsu H3167 PMTs. Table 2.1 gives parameters on hodoscopes including FP. Hits in FP elements 1-12 (those below and out of the beam) are part of triggers that select interesting events in the spectrometer. Thus FP, along with BP, serves to define the geometric acceptance of the spectrometer. Triggers are described later in Section 2.6.1.

Drift chambers FD0-3

Four drift chambers (FD0-3) were placed in the forward region of the spectrometer. Table 2.5 gives the specifications for the FD chambers. Note FD0 had only one double-plane of y information, as opposed to the three double-planes of FD1-2. Unlike the ID chambers, the FD's wire planes were arranged to give the best measurement resolution along the y axis, as the 48D48 spectrometer sweeps particles vertically. FD3 was situated inside the 48D48 magnet. The chambers used a fill gas consisting of 76% argon, 20% isobutane, and 4% methylal.

Chamber	Planes	Rotation Angle	Spacing (mm)	Location(mm)			Resolution (mm)	channels
				x	y	z		
FD0	$y-y'$	90°	5.08	0.0	-43.0	20.0	0.50	24×2
	$u-u'$	210°	5.08				0.15	48× 2
FD1	$v-v'$	150°	5.08	-0.23	-67.2	306.2	0.15	48×2
	$y-y'$	90°	5.08				0.15	48×2
	$u-u'$	210°	5.08				0.15	48×2
FD2	$v-v'$	150°	5.08	-1.3	-67.6	666.6	0.15	48×2
	$y-y'$	90°	5.08				0.15	48×2
	u	150°	12.7				0.30	64
FD3	$y-y'$	90°	12.7	2.19	-35.9	1481.4	0.30	64×2
	v	30°	12.7				0.30	64

Table 2.5: Specifications of the FD chambers. The rotation angles are defined in Fig. 2.5. 'Spacing' denotes the chamber sense wire spacing, 'Location' refers to the position of the center of the chamber, and 'Resolution' is the position measurement resolution.

2.3.2 48D48 magnet

The heart of the spectrometer used in experiment 885 was the 1.4 Tesla 48D48 magnet; a dipole magnet with a field parallel to the x-axis, so that it deflected particles vertically. The magnet's name comes from its pole face, which measures 48" × 48". This large acceptance dipole has a 31.5" gap, and was situated at z=2.00 m.

In order to reduce multiple scattering of secondaries through the spectrometer, the volume of the magnetic field within the magnet was enclosed in two bags made of thin plastic and filled with ^{4}He, one upstream of FD3, and one downstream.

2.3.3 Back region

The back region of the E885 spectrometer (Fig. 2.4) consists of two large drift chambers BD1-2, a Čerenkov detector BC to veto pions, the scintillator hodoscope BP which defines spectrometer acceptance, and the back timing wall BT.

Drift chambers BD1-2

Particle tracking downstream of the 48D48 magnet is accomplished with 2 large drift chambers, BD1 and BD2, built by the University of Freiburg group [52, 53]. Reconstruction of the scattered particle tracks through the spectrometer is accomplished by matching tracks in the FDs with tracks in the BDs. Given the known field of the 48D48 magnet, the momenta of the scattered particles can be determined.

The BDs have an active area (width × height) of 1.1400 × 2.140 m^2, and are aligned at an angle of 30° to the y-axis, so that the plane of the detectors is approximately perpendicular to the scattered K^- trajectories. Table 2.6 gives more parameters of the BD chambers. Combined, the two chambers have 9 planes of hit information from which to reconstruct a straight line track in the back

Chamber	Planes	Rotation Angle	Spacing (mm)	location(mm)			Resolution (mm)	channels
				x	y	z		
BD1	u	120°	20.0	-3.4	685.9	3731.7	0.30	128
	v	60°	20.0				0.30	128
	$y-y$'	90°	20.0				0.30	112×2
BD2	u	120°	20.0	-0.4	693.9	4558.9	0.30	128
	$v-v$'	60°	20.0				0.30	128×2
	$y-y$'	90°	20.0				0.30	112×2

Table 2.6: Specifications of the BD chambers. The rotation angle is defined in Fig. 2.5. 'Spacing' denotes the chamber sense wire spacing, 'Location' refers to the position of the center of the chamber, and 'Resolution' is the position measurement resolution.

region. The fringe field of the 48D48 magnet was approximately 0.5 - 1.0 gauss, at a distance of 1 m from the face of the magnet. The gas mixture used was 76% argon, 20% isobutane, and 4% methylal.

Čerenkov detector BC

Discrimination between K^+s and π^+s downstream of the 48D48 is performed by the Čerenkov detector BC. Situated between drift chamber BD2 and scintillator hodoscope BP, BC ensures that pions in the back region are rejected. Fig. 2.6 shows a schematic of the detector, and Table 2.2 gives some parameters. BC consists of 3 layers of 54 blocks each of silica aerogel (totalling 162 blocks), with an index of refraction of n=1.04. Čerenkov light is reflected by aluminized mylar, onto the photocathodes of 20 RCA8854 PMTs. Kaons may decay en route to BT, and BC (with an active area matched to scintillator BP), makes this less likely to go undetected. BC was shown to be 98.5% efficient [54]. The detector is inclined at 30° to the y axis, so that particle tracks are roughly perpendicular to the plane

of the detector.

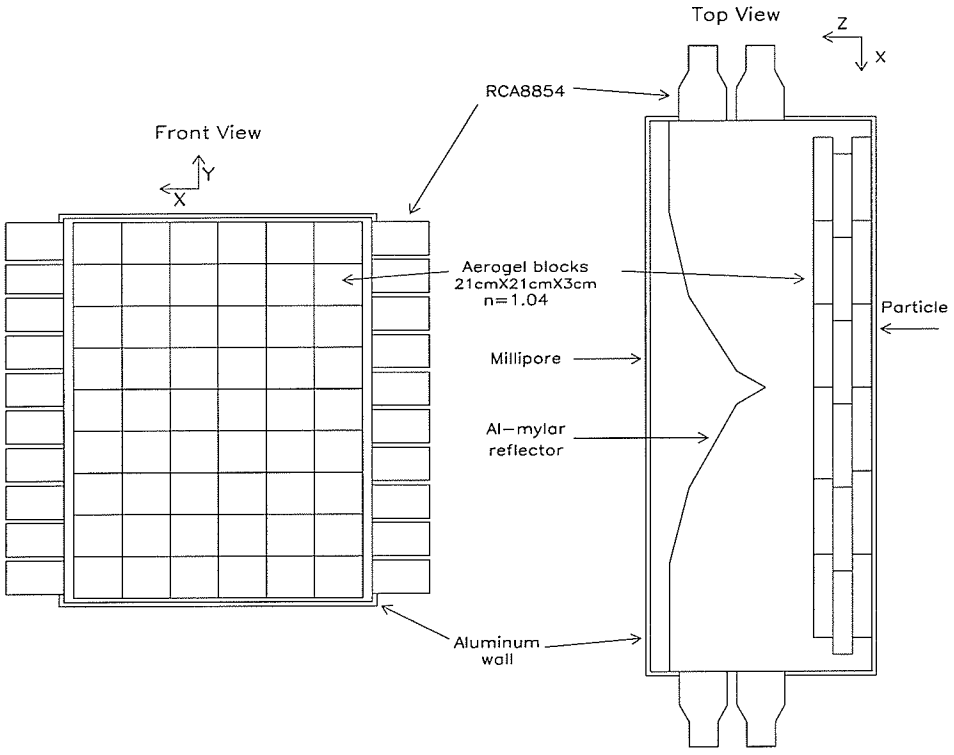

Figure 2.6: Schematic drawing of Čerenkov detector BC.

Scintillator hodoscope BP

In the back region, downstream of the 48D48 magnet, the spectrometer acceptance is defined by the scintillator hodoscope BP. Consisting of six vertically oriented slats to give horizontal position information, the active area of BP is matched to that of the Čerenkov detector BC to ensure proper PID. Table 2.1 lists the salient features of detector BP. Each slat is viewed from either end by 50.8 mm diameter Hamamatsu H1949 PMTs. The detector was oriented at 30° with respect to y-axis to ensure that secondary particles were incident roughly normal to the plane of BP. The center of BP was located at $x = 13.0$ mm, $y = 1.064$ m, and $z = 5.244$ m. Horizontal angular coverage of BP was $\mid \theta_x \mid \leq 6.4°$.

Timing hodoscope BT

The final detector in the E885 spectrometer array is the back timing wall, or BT. Details of this high-resolution TOF detector can be found in [55]. Some parameters are given in Table 2.1. BT consists of 40 bars of BC408 scintillator, viewed at either end by 5.08cm diameter Hamamatsu H1949 PMTs. The detector itself was inclined at 15° to the y axis (individual bars were rotated approximately 25° to the y axis; the rotation angle varied slightly with bar number). The reduced pitch angle of the detector was indicated by Monte Carlo studies; for a particular particle type, the TOF spread over a given BT element is minimized by selecting an inclination angle of 15°, and the separation between K^+'s and protons for the second-level trigger (discussed below) is maximized.

Note that some K^+s may decay downstream of BC, to μ^+s or π^+s. In order to discard these events, cuts are made on tracks projected through the BD chambers to BT, when compared with actual hit information in BT. In this way most decays downstream of BC (which distinguishes between kaons and pions) are rejected.

The centre of the BT scintillator was located at x = -11.0 mm, y = 0.567 m, z = 7.801 m.

2.4 Out-of-beam detectors

In the Forward region of the spectrometer, there are two detector systems which are not related to the workings of the spectrometer, but integral for detecting decay particles from candidate S=-2 systems. These are the out-of-beam detector systems; the Scintillating Fibre Arrays, or SCIFI, and the neutron counters.

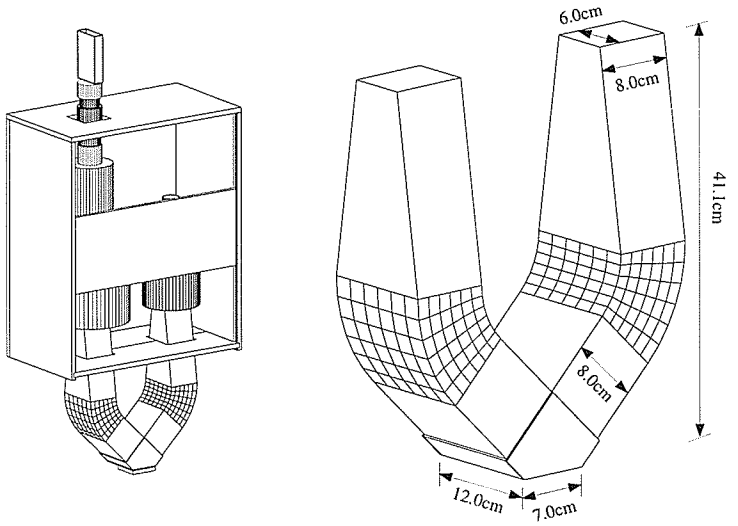

Figure 2.7: Schematic view of a scintillating fibre block. Intensity information in particular fibres is read out from the end of each arm, yielding orthogonal views of particles traversing the blocks.

2.4.1 Scintillating fibre detectors (SCIFI)

Scintillating fibre (SCIFI) detectors were employed to detect and track decay particles emanating from the target. Two SCIFI detectors each with two arms were constructed for the experiment, and situated one above and one below the target. A SCIFI detector consisted of 7600 fibres (100 layers of 76 fibres), arranged in a U-V configuration, connected to a multi-stage image intensifier (IIT), and a camera-lens/DALSA[1] CA-D1 CCD camera system to record the image. Fig. 2.7 is a schematic of a SCIFI block.

The fibres used were Bicron[2] BCF-12 1mm $\times$ 1mm square polystyrene scintillator. Individual fibres were clad in a layer of acrylic to promote internal reflection, and then painted to reduce cross-talk.

Each leg of the block is connected to an image intensifier with three stages of

[1]DALSA Inc., Waterloo, ON, Canada
[2]Bicron, Newbury, OH, U.S.A.

amplification. The second and third stages of amplification consisted of gateable micro-channel plates. A second-level trigger was employed in the decision to read out the IITs, gating these stages and preventing image saturation. Prior to the completion of the second-level trigger decision, the image of an event is stored on a phosphor screen.

Light from the IIT is demagnified and focussed by a conventional camera lens system onto the the 256 $\times$ 256 pixel array (4.096 mm $\times$ 4.096 mm) of a Dalsa CCD camera unit. While this camera is capable of an image rate of 200 Hz, a limit of roughly 60 Hz was imposed due to a reduction in the quality of the IIT data at higher rates.

Much of the data passed from the CCD consisted of null data in the form of zeros. Zero suppression was then added to the CMU-built "Big Boards", in order to reduce the number of words written to tape per event.

The quality of the SCIFI images was sensitive to environmental factors including heat and humidity. Background noise increased during running periods of high humidity, common during the summer months at BNL.

2.4.2 Neutron counters

The neutron counters were arrays of plastic scintillator arranged vertically on the left and right sides of the target (denoted LN and RN, respectively). The counters were intended to detect neutrons emitted during the formation of double-Λ hypernuclei as per Equation 1.6. Each neutron array consisted of 5 rows of 10 scintillator bars hung vertically. A single bar was composed of BC408 scintillator, with the dimensions 152.4 mm wide, 50.9 mm thick, and 1.8288 m high. Between the target and each neutron array was situated a thin plastic scintillator veto (segmented in a similar fashion to of the neutron detector bars), to eliminate spurious background counts from charged particles.

The neutron counters are not used in the analyses of this thesis. A more complete description of the neutron arrays can be found elsewhere [56, 50]. An analysis of the neutron spectrum in Experiment 885 and limits on the cross-section for production of double-Λ hypernuclei via $(\Xi^-, {}^{12}C)_{atom} \rightarrow {}^{12}_{\Lambda\Lambda}B + \mathrm{n}$ has been accepted for publication [57].

2.5 Targets

Two targets were used for production mode data acquisition during the 1996 E885 run. Initially, CH_2 was installed as the Ξ production target. In this configuration, Ξ^--baryons are created in the CH_2 target, then a subset of them propagates through a tungsten degrader, slows down, and stops in the scintillating fibre bundles, to form S=-2 exotic systems. After one month of running in this configuration, a target switch was made to a chemically vapour deposited (CVD) diamond target. In the latter configuration, the diamond serves both as a production mechanism for the Ξ-baryon, and absorption target for the slowed Ξ^-. The diamond target has a low mass number (A = 12), and high density ($\rho = 3.3$ g/cm^3), advantageous for producing a large Ξ^- yield. The forward-angle cross section of quasi-free $p(K^-, K^+)\Xi^-$ scales by $\mathrm{A}^{0.38}$ [58], so that targets with a small mass number are satisfactory for producing a large Ξ^- yield. Diamond has the highest density of the low mass number materials, important for stopping the short-lived Ξ^--baryons.

2.5.1 CH_2

The CH_2 block had dimensions of 77 (x) $\times$ 10 (y) $\times$ 130 (z) mm^3, and was sandwiched between tungsten degraders and the SCIFI devices above and below the beamline. The density of the polyethylene target was 0.94 g/cm^3. The target thickness, can be separated into contributions from carbon, and hydrogen. The

thickness due to carbon was 5.25×10^{23} cm^{-2}, while the thickness due to hydrogen was 10.5×10^{23} cm^{-2}.

2.5.2 Diamond

The target used for the majority of the E885 run time was assembled from layers of chemical-vapour deposited diamond, epoxied together to a volume of 80 (x) $\times$ 10 (y) $\times$ 50 (z) mm^3. Details of the target and fabrication are given in Ref. [59]. Ten wafers of CVD carbon 10 mm $\times$ 10 mm $\times \sim$ 1 mm were stacked together and epoxied into a 1000 mm^3 cube. Forty such cubes were assembled and epoxied together to produce the rectangular target. The target has a density of $\rho = 3.3$ g/cm^3, that is, approximately 93% of the density of single-crystal diamond. The target thickness, can also be separated into contributions from carbon (diamond), and hydrogen (contamination due to the epoxy), as was done for CH_2. The thickness due to carbon was 8.27×10^{23} cm^{-2}, while the thickness due to hydrogen was two orders of magnitude smaller, approximately 7.6×10^{21} cm^{-2}. The target was situated during the experiment at x = 0.0 mm, y = 0.0 mm, and z = -200.0 mm.

2.6 Triggers

2.6.1 First-level triggers

Beam particles incident on the target region are identified by the four-element hodoscope IT, and the Čerenkov detector IC:

$$K_{beam} = \mathrm{IT} \cap \overline{\mathrm{IC}} \tag{2.1}$$

$$\pi_{beam} = \mathrm{IT} \cap \mathrm{IC} \tag{2.2}$$

Secondary particles that are scattered into the spectrometer are identified as K_{scat} or π_{scat}, using hodoscopes FP and BP, and the discriminated signals from Čerenkov detectors FC, FC0 and BC.

$$K_{scat} = \mathrm{FP} \cap \mathrm{BP} \cap \mathrm{FC0} \cap (\overline{\mathrm{FC} \cup \mathrm{BC}}) \tag{2.3}$$

$$\pi_{scat} = \mathrm{FP} \cap \mathrm{BP} \cap (\mathrm{FC} \cup \mathrm{BC}) \tag{2.4}$$

Note that a signal is demanded from FC0 when forming the K_{scat} trigger. This requirement rejects a portion of the proton contamination in the scattered beam, as described in Section 2.3.1. Čerenkov detectors FC and BC are used in veto mode, and a K_{scat} is formed only if no signal is found in these detectors.

The main experimental triggers in E885 are then assembled from the simpler triggers above, namely:

$$KK = K_{beam} \cap K_{scat} \tag{2.5}$$

$$KKM = K_{beam} \cap K_{scat} \cap \mathrm{Matrix} \tag{2.6}$$

$$\pi K = \pi_{beam} \cap K_{scat} \tag{2.7}$$

$$K\pi = K_{beam} \cap \pi_{scat} \tag{2.8}$$

$$\pi\pi = \pi_{beam} \cap \pi_{scat} \tag{2.9}$$

Table 2.7 gives the triggers and the prescale factors.

2.6.2 Second-level trigger and matrix

Memory lookup unit (MLU) second-level trigger

The initial online selection for (K^-, K^+) events is done by a series of hardware measurements such as Čerenkov detectors and rapid TOF calculations. However,

Trigger	Definition	typical value	
		Counts/spill	Prescale factor
K_{beam}	IT$\cap\overline{\text{IC}}$	8×10^5	8×10^5
π_{beam}	IT$\cap$ IC	6×10^6	2×10^6
K_{scat}	FP$\cap$BP $\cap$ FC0 $\cap\overline{(\text{FC} \cap \text{BC})}$	-	-
π_{scat}	FP$\cap$BP$\cap$(FC $\cap$ BC)	-	-
$K\pi$	$K_{beam} \cap \pi_{scat}$	150	1×10^3
πK	$\pi_{beam} \cap K_{scat}$	15	4×10^1
KK	$K_{beam} \cap K_{scat}$	100	1×10^0
KKM	$K_{beam} \cap K_{scat}\cap$ Matrix	50	1×10^0
ITBT	IT $\cap$ (BT$_a$ $\cap$ BT$_b$)	6.6×10^3	2×10^3

Table 2.7: Definitions of E885 triggers. Scaler values of counts/spill and their respective prescale factors are shown for typical run conditions of $\sim 6 \times 10^{12}$ protons/spill on the primary Pt target.

despite these first level identifications of K^+'s, the trigger rate would still be dominated by misidentified protons from elastic and inelastic K-p scattering. A second-level trigger is necessary to reduce events in which protons scatter into the spectrometer.

Prior to E885, experiments on D6-line (E813/836) made use of a software/hardware second-level trigger, to reduce K-p scatter. This decision took $\approx 150\mu$s to complete; too long for requirements of the SCIFI/IIT detectors. Thus a faster 2nd level trigger was created entirely in hardware. A LeCroy[3] 2372 MLU or memory lookup unit was employed to this end.

The E885 spectrometer has a large acceptance, so secondary particles have a great variety of momenta and path lengths through the back region. Thus, no single TOF cut will adequately distinguish between secondary K^+ and protons; the acceptance must be broken up into smaller bites in order to apply TOF cuts to more constrained regions.

Secondary tracks in the spectrometer are classified in terms of FD3 cluster (a y-position grouping inside the 48D48 magnet), and BT log number (y-position at the back wall of the spectrometer). This breaks the spectrometer acceptance into smaller regions, such that a single TOF cut per region is valid.

A rough estimate of particle momentum is established by the event FD3 cluster and BT log hit. From this, a TOF cut can be made to eliminate excess protons. The MLU-based second-level trigger decision rejected $\simeq 96\%$ of secondary protons allowed via the first-level trigger, while retaining $\simeq 100\%$ of the outgoing K^+s. Furthermore, the MLU second-level trigger was not applied to approximately 1.5% of the events, in order to monitor particle identification and ensure against biasing of the acquired data set.

[3]LeCroy Corp., Chestnut Ridge, NY, U.S.A.

The matrix

The IIT system required low rates for quality images, hence an attempt was made to clean up the KKIIT trigger as much as possible. To this end a hardware matrix was employed, using the same philosophy as the second-level trigger. A given event was classified according to FP element (y-position prior to 48D48 magnet), and BT-log (y-position at back wall). A cut on regions of FP vs BT further reduced the IIT trigger rate.

Chapter 3

Microstrip Gas Chambers

3.1 Introduction

In this chapter we report on the development and testing of a specific detector subsystem, the microstrip gas chamber (MSGC) vertex detector. The microstrip detectors constitute the major hardware component of the thesis. The design used in experiment 885 was a second-generation one, the performance of which was reported on in [60]. Prototypes of a first-generation MSGC were built and tested; we report on these in Appendix A.

While microstrip gas chambers were first introduced over a decade ago [51], they have only rarely been used in experiments [61, 62, 63]. More commonly, tests of MSGCs are performed in idealized laboratory settings either on the bench, or by in-beam tests. Reviews of the subject are available elsewhere [64, 65]. Given the exceptional rate capabilities of MSGCs ($\geq 10^6$ mm^{-2} s^{-1}), it is anticipated that they will be utilized in high-luminosity experiments, provided they can be shown to have sufficient longevity.

In this chapter we report on MSGCs utilized in the harsh environment of an experiment. Microstrip prints, which constitute the active area of the MSGC, were

manufactured with two distinct photolithographic processes, integrated circuit and printed circuit technology (denoted IC and PC, respectively). Both IC and PC prints with an active area of 80×50 mm^2 were used in the 1996 E885 run at BNL. IC-type prints have advantages such as excellent line tolerance ($\pm 0.5 \mu$m) and narrow attainable trace widths, but may be prohibitively expensive. PC versions of microstrip prints [66, 67] are cheaper and more durable, but suffer from limits on trace width and poorer line tolerances. PC fabrication can occur on a much larger size scale ($\sim$ 1 m^2), important for applications in large-area experiments that can accommodate the reduced spatial resolution of PC prints.

In the next section we will detail the different types of microstrip prints used in our MSGCs. The chamber layout is described in section 3, followed by a description of the signal readout electronics, and the related noise sources and shielding efforts in sections 4 and 5, respectively. We then report on beam and bench tests conducted at TRIUMF, as well as the performance of 3 chambers utilized in experiment 885 at Brookhaven National Laboratory.

3.2 Microstrip prints

Two types of microstrip prints were utilized in the experiment, fabricated on flexible Upilex[1] and Kapton[2] film. Flexible plastics have advantages over glass substrates in that they are easily handled and readily shaped and curved for specific detector designs. Furthermore they are a lower Z material and hence cause less energy loss and multiple scattering of incident particles. IC prints consisted of a thin gold layer sputtered on Upilex, then etched[3]. The substrate for the PC

[1]Upilex polyimide film is manufactured by UBE Industries, Japan, and distributed by ICI in the United States.

[2]Kapton polyimide film is manufactured by DuPont, Wilmington DE, U.S.A.

[3]lithography by PPM Photomask Inc., Montreal PQ, Canada.

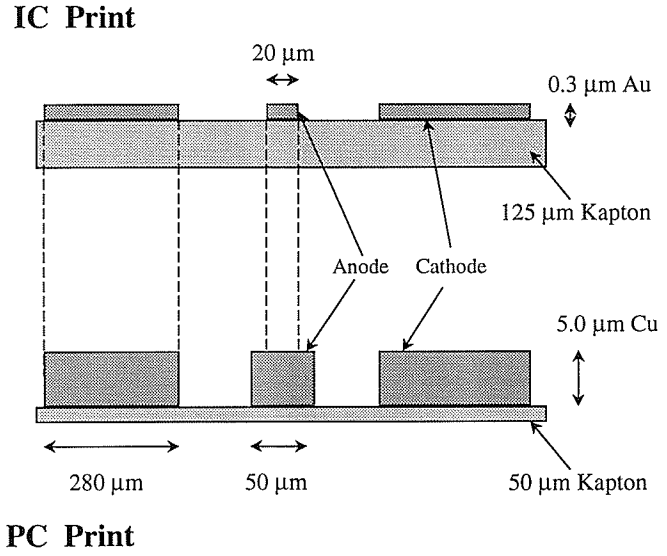

Figure 3.1: Schematic layout of the 2 different type of microstrip prints, IC and PC (drawing is not to scale).

prints consisted of off-the-shelf Novaclad[4] flexible copper-on-Kapton laminate[5]. Table 3.1 compares and contrasts the geometries of the two types of prints used in the experiment, while Fig. 3.1 shows a cross-section of the microstrip prints, indicating the differences of the two print geometries.

Print Type	Substrate	Substrate Thickness (μm)	Metallic Layer/Thickness (μm)	Cathode (μm)	Anode (μm)	Pitch (μm)
IC Prints	Upilex	125	Au/0.3	280	20	500
PC Prints	Kapton	50	Cu/5.0	280	50	500

Table 3.1: Comparison of geometry of IC and PC based microstrip prints.

[4]Novaclad FLX220002180 by Sheldahl Inc., Northfield MN, U.S.A.

[5]lithography by Precision Art Coordinators, Inc., East Providence RI, U.S.A.

3.2.1 IC prints

The IC prints consisted of a 0.3 μm thick gold layer deposited on 125 μm, high quality type-S Upilex. The gold layer was then etched using a wet-etch process according to the patterns in Fig. 3.2. Two masks were utilized; one for x readout (Fig. 3.2 a), and one for y (Fig. 3.2b). The geometries for the different masks are similar in terms of their charge amplifying structures, but are read out differently. An IC x print consists of 160 anodes of 20 μm width, interleaved with 161 cathodes of 280 μm width. The strip pitch is 500 μm. Anodes are grouped and read out in pairs, so that the readout pitch in x is 1 mm. An IC y print has 96 anodes of 20 μm width interleaved with 97 cathodes of 280 μm width. As IC y anodes are not paired, the readout pitch is 500 μm. Roughly 80% of the strips on these medium-sized prints (active area 80×50 mm^2) were defect-free. The 20% of the strips that were problematic suffered from lithographic defects such as open traces, metallic protuberances from anode or cathode structures, or metal islands possibly due to localized incomplete etching. Such problem sites limit the overall absolute efficiency of the chamber.

3.2.2 PC prints

The second type of print was manufactured using conventional printed circuit technology. Minimum tolerances in PC processing are typically poorer than IC processing (eg. larger minimum line width, larger pitch). However, the PC prints suffered from fewer gross defects such as open traces and metal islands ($\sim$5% of strips on a given PC print had defects, vs. $\sim$20% of strips on an IC print). The PC prints used a Novaclad flexible material consisting of 5 μm thick Copper deposited on 50 μm Kapton. The Cu/Kapton laminate is said to be "adhesiveless", which proved problematic to etch. Prior to depositing Cu onto the Kapton, a conducting chrome seed coat is laid down. Thus when the initial prints were returned from the manufacturer, with the Cu etched and the seed coat exposed, there was

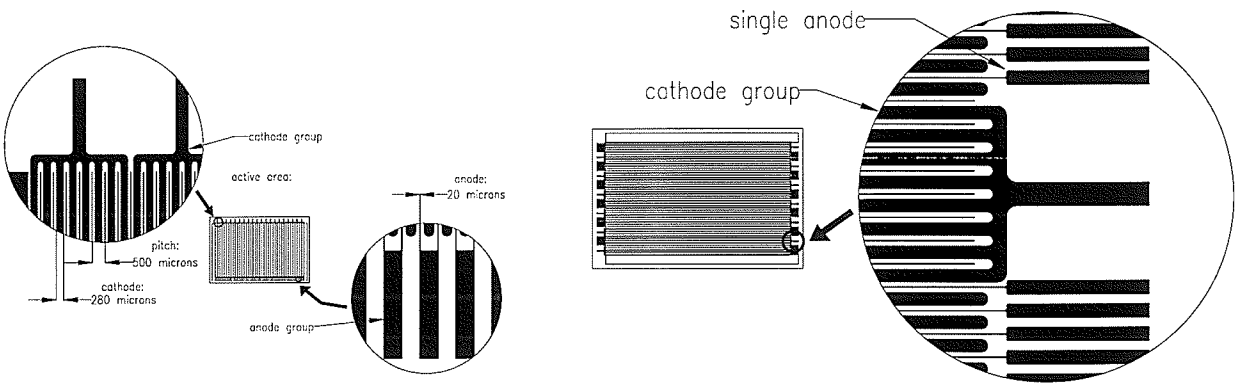

Figure 3.2: a) Lithographic design of the IC x print layout, with details highlighted. Cathodes of width 280 μm are taken out in groups of eight at the top, while 20 μm anodes are read out in pairs at the bottom. b) Design of the y print layout. Single anodes are read out on left and right sides of the print, alternating with cathode groups.

essentially zero resistance between anode and cathode structures. Prints had to have a secondary-etch to remove the chrome seed coat[6]. The PC prints had similar geometries, in both x and y, as the IC prints, with the exception of the anode width. Printed circuit technology limited traces to a minimum width of 50 μm, so the anodes in the PC x and PC y masks were roughly doubled to 50 μm. The second major geometrical difference is the thickness of the metallic layer; 5 μm of Cu represents a 17-fold increase in height of the charge amplifying structure. The thicker traces are better able to withstand the effects of discharge than the more delicate sputtered gold traces of the IC prints.

[6]Note Sheldahl is replacing the 2200 series Novaclad, which has a chrome seedcoat between the Kapton substrate and the Copper, with a 2300 series, which has no chrome seedcoat.

3.2.3 Passivation

Short-term gain instability in MSGCs is caused by polarization of the substrate, and charge deposition on the substrate[68]. Solutions to this problem include (i) use of a high resistivity substrate such as Schott S-8900 glass[7] (ii) 'ion-implantation' on and under the surface of the substrate, (iii) pre-etch chemical vapour deposition of diamond film on boro-silicate glass [68] (iv) passivation of the print with a post-etch metallic oxide layer. Note that we do not utilize a backplane voltage (an electrode deposited on the opposite side of the substrate to that of the anode and cathode structures) as this is unnecessary in the presence of a high-resistivity layer on the substrate[69]. Both IC and PC prints were passivated with a post-etch thin nickel-oxide layer in order to conduct charges deposited on the print surface to the electrodes, avoiding charge buildup. The NiO layer may have some additional functions[70]. For example, the passivation layer acts as a protective coating between the substrate and the active ions in the avalanche region. Furthermore, in the event discharges are caused by secondary electrons, the low secondary electron emission coefficient of NiO will reduce the probability of sparking.

After etching, all prints were passivated with a Ni/NiO overcoating, according to the procedure established in ref. [70]. A d.c. sputtering machine[8] backfilled with Ar at 100 mTorr was utilized to deposit a nickel layer over the etched microstrip prints. Approximately (40 $\pm$ 20%) of the nickel is oxidized, producing a (50 $\pm$ 15) nm thick, high resistivity layer of 10^{13}-10^{15} $\Omega/\Box$.

3.3 Packaging/board layout

Microstrip prints were mounted on an etched FR4 (fire-retardant G-10) board with a cutaway near the centre. As shown in Fig. 3.3, an IC x print is mounted

[7]Schott Glass Technologies Inc., Duryea PA, U.S.A.

[8]Consolidated Vacuum Corporation vacuum chamber, type CVE-15.

on an FR4 board. Electrical connection from the print to the board is made via Monosotropic Heat-Seal Connectors (HSC)[9]. The HSC are applied to the microstrip print and FR4 board and a mechanical and electrical connection is made with pressure and heat via a bonding machine[10]. In order to conserve space along the axis of the beam, x and y prints are mounted back-to-back on opposite sides of the FR4 board, so that a single board acts as an integrated (x,y) chamber. Signal traces run to a pair of on-board preamplifier cards, the QPA02. The latter is a 128-channel monolithic preamplifier card constructed for silicon vertex detectors at Fermilab [71].

An attempt was made to keep the traces on the FR4 board (carrying the unamplified signal from the microstrip print to the QPA02 preamplifier) as short and wide as possible. However spatial constraints due to other detectors in the beamline necessitated that the preamps and signal cables exit below the gas volume, thereby extending the trace fanout considerably. In order to provide a good common ground, an internal ground plane was provided in the multilayer FR4 board.

The x and y prints are enclosed in a gas chamber consisting of connected x and y volumes. The gas mixture flows through the x volume, between the prints and then out the y volume to ensure the full chamber is properly flushed. The gap between the drift electrode (a plane of 50 μm aluminized mylar) and the microstrip print was 5 mm. Fig. 3.4 depicts a cross-sectional top view of an MSGC, indicating the back-to-back configuration of the prints and the connected gas volumes.

[9]The HSC are manufactured by Nippon Graphite Industries, Ltd., Japan, and distributed by Elform of Reno NV, U.S.A.

[10]Man U Bond Heat Seal Press Model 007, Elform, Reno NV, U.S.A.

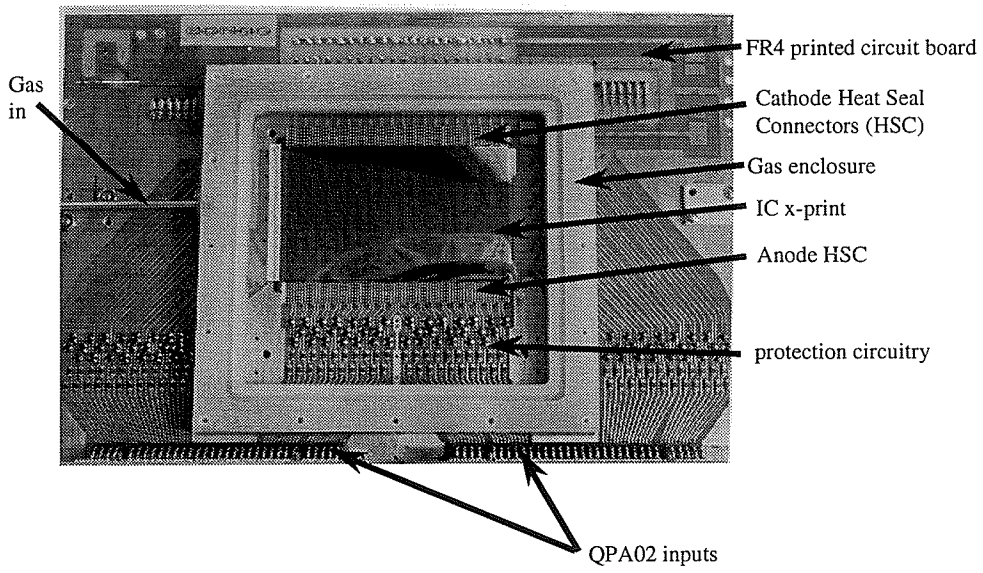

Figure 3.3: Photograph of x print mounted on an FR4 board. Prints are housed in a G10 enclosure which is glued to the FR4 board. A drift plane, not shown, is mounted over the microstrip print.

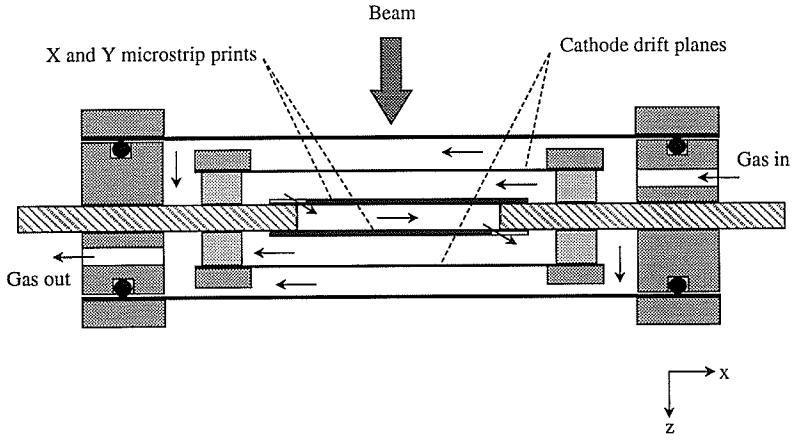

Figure 3.4: Cross-section of MSGC. The thin arrows denote gas flow (drawing is not to scale).

3.4 Setup electronics

The MSGCs use a preamplifier and a postamplifier/receiver card to amplify the signals from the anode strips and convert the QPA02 differential signal to single-ended output. Signals from the anodes are passed via heat-seal connectors to the FR4 board, through protection circuitry and then to the preamplifier card. The 128-channel preamplifier card used a semi-custom application specific integrated circuit (ASIC) called the QPA02, each chip containing 8 channels. The QPA02 is a high speed bipolar transimpedance amplifier built using a Tektronix Quickchip semi-custom process[71] and provides a differential output which is taken on ribbon cable to a rack of TRIUMF-built receiver cards. The receiver cards used Motorola MC10115[11] quad line receivers to provide 32 channels of single-ended output. The test circuit depicted in Fig. 3.5a was used to measure a gain curve for the readout system, and Fig. 3.5b shows the measured gain curve. The charge gain was 44 mV/fC and the equivalent noise charge was about 2000 electrons. A delta function pulse into the amplifier chain had a 10% to 90% risetime of 8 ns and a falltime of 28 ns, with a full width of approximately 50 ns.

In total, for the 3 chambers, 528 channels were instrumented, including 240 channels in the x direction and 288 in the y direction.

3.5 Noise/shielding

The microstrip/QPA02 system proved to be extremely sensitive to noise sources. In the quiet conditions of bench-testing at TRIUMF, most of the noise was eliminated by a simple copper shield over the QPA02 preamp top surface inputs. However in the harsher environment of the Brookhaven AGS D6 experimental area, more drastic measures were required.

[11]Motorola Literature Distribution, P.O. Box 5405, Denver CO, U.S.A. 80217, or, http://motorola.com/sps

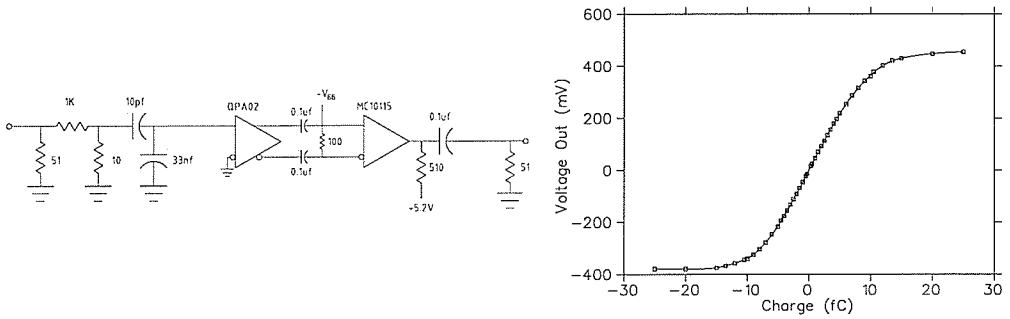

Figure 3.5: a) Schematic of test circuit used to measure the QPA02 gain curve in Fig. 3.5b. b) QPA02 gain curve.

The most significant reduction in RF noise was obtained by shielding the QPA02 inputs from the outputs, in the form of an RF gasket as suggested by Yarema and Zimmerman[72]. This was essential in removing oscillations at the 64 MHz pole of the QPA02.

Faraday cages were constructed to limit radiative RF noise from external sources. Sensitivity to external noise sources varied for a variety of reasons which included ambient temperature and RF noise from the accelerator. Only one noise source could not be completely eliminated: an integral component of the experiment was a set of four CCD camera devices (see Section 2.4.1). A TTL digital clock signal associated with the CCD cameras broadcast RF noise that was detected by the MSGCs, necessitating high discriminator thresholds. This reduced the overall efficiency of the chambers by approximately 10%.

3.6 TRIUMF bench and beam tests

Bench tests included a variety of pulse height measurements, cosmic ray efficiency studies and measurements with an ^{55}Fe source. One of the latter measurements is shown in Fig. 3.6. Depicted is a pulse amplitude spectrum of X-rays, emitted by an ^{55}Fe source, as measured by an IC MSGC using a gas mixture of argon/isobutane

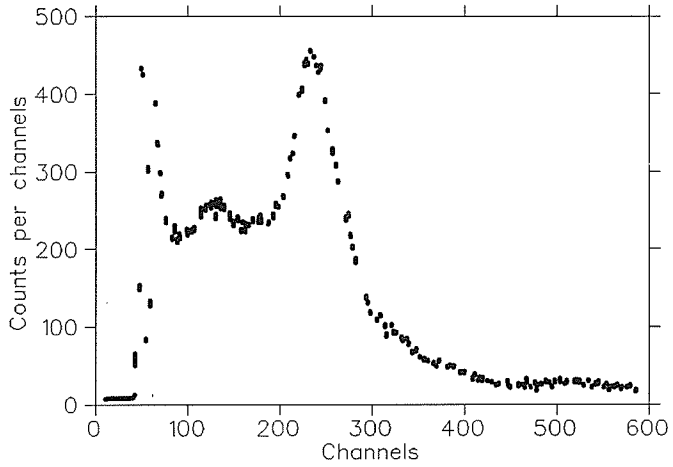

Figure 3.6: Pulse amplitude spectrum of ^{55}Fe X-rays, recorded by an IC MSGC using a gas mixture of argon/isobutane (90:10). The main 5.9 keV ^{55}Fe peak is to the right, while the escape peak is seen as the central bump in the spectrum .

(90:10).

Beam tests

The M13 beamline at TRIUMF is a secondary channel that collects π, μ and e from a 10 mm graphite target and momentum selects them with two dipoles and seven quadrupole magnets. Its total length from production to target focal point is 11 metres. We operated the channel at 100 MeV/c momentum with a large aperture and positive polarity. The total rate at this momentum was 10^5 particles/sec of which approximately 70% were π^+, 30% e^+ and a very small number of μ^+. Time-of-flight from the production target to trigger scintillators was employed for particle identification: Fig. 3.7 shows a TDC spectrum of events indicating the arrival time difference between π^+ and e^+. The start signal was provided by the scintillator coincidence and a stop signal was provided by the RF of the TRIUMF cyclotron. This RF signal is synchronous with the primary proton beam, thereby allowing a time measurement of the secondary particles.

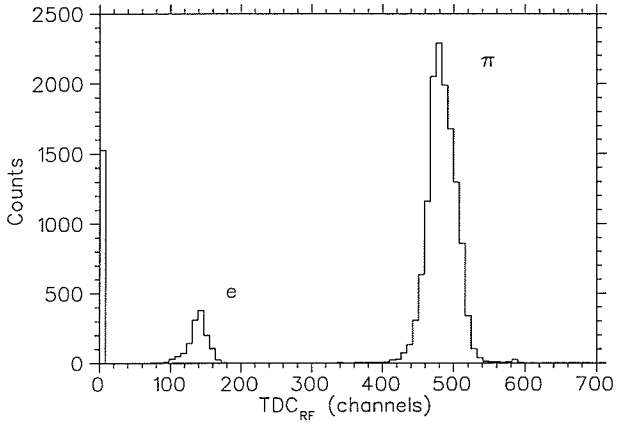

Figure 3.7: A TDC spectrum of events indicating the arrival time difference of e^+ and π^+.

Four MSGCs were mounted on a table in the beam, and three scintillators in front and behind were inserted and used to define the particles traversing the detectors. The coincidence signals of these scintillators were also used as the trigger signal and defined the timing of the events, as described above

Fig. 3.8 shows an efficiency curve for an IC x print mounted in the TRIUMF test beam. The curves are for a subset of the print as only 16 channels were instrumented for the test. The strips were chosen for good quality lithography and hence the efficiency represents the optimal inherent property of the prints and associated electronics. Discriminator thresholds are set at 50 mV. Under these ideal conditions, efficiencies of ~99% for minimum ionizing particles are attained. Once the entire print is instrumented, the absolute efficiency suffers due to several complications, including lithographic defects.

3.7 Performance during the experiment

As described in Chapter 2, the AGS accelerates protons to 24 GeV/c and then directs them onto a platinum production target, sending K^-, π^-, and anti-protons

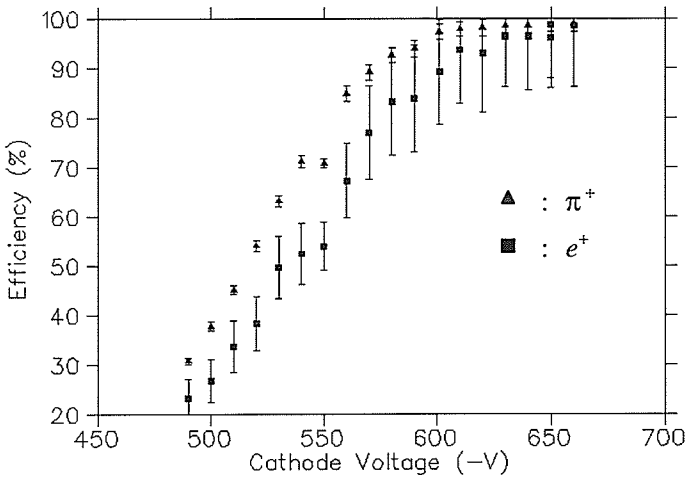

Figure 3.8: Efficiency curves for IC x print in the TRIUMF M13 beam test.

down the D6 beamline. Secondary particles are selected through two stages of electrostatic separation, and brought to a final focus in the E885 target area. Recall that in-beam MSGCs are mounted upstream (IM1) and downstream (FM1 and FM2) of the diamond target, as depicted in Fig. 3.9. Drift chambers ID1-3 and FD0-3 provide tracking for beam and scattered particles upstream and downstream of the target; the MSGCs were used to improve knowledge of the interaction vertex. The gas mixture used in the MSGCs at BNL was argon/dimethyl ether (DME) (80:20).

PC x and IC y prints were mounted in the upstream MSGC IM1. Downstream of the target, chambers FM1 and FM2 contained only IC prints (IC x and IC y). Commissioning of the detectors was lengthy due to the difficulties in eliminating oscillations in the QPA02 preamplifiers and shielding against RF noise sources. Once commissioned, the detectors operated more smoothly, although sparking occurred on particular prints at regular intervals. On occasion regular sparking necessitated reducing the chamber operating voltage.

Fig. 3.10 shows efficiency data for a PC x print, taken during the 885 experiment, with the entire print instrumented. For comparison, the operating point for

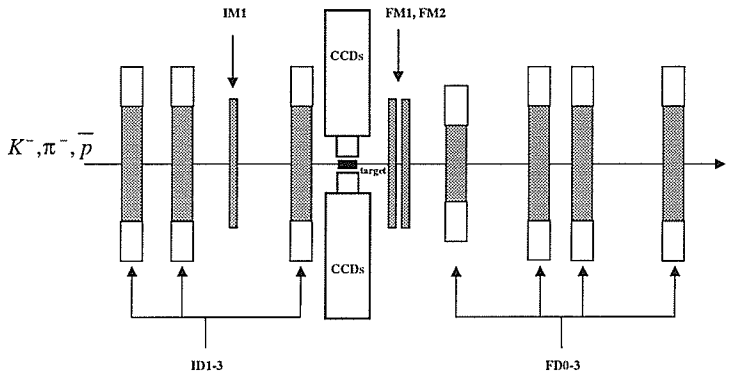

Figure 3.9: Position sensitive detectors in BNL-E885. For clarity, not all detectors in the target region are shown. MSGCs are IM1 and FM1-2. Drift chambers include ID1-3, FD0-3 (diagram not to scale).

IC x and y prints is shown. Note that due to the much thicker Cu metal layer and wider anode structure of the PC x print, compared to the Au on Upilex IC x print, the PC x microstrip will plateau at a higher operating voltage (plateau voltages could not be achieved due to breakdown beyond V_{x_μ}=640V). The experimental results include known defects due to lithography and high thresholds due to the CCD camera noise (discriminator thresholds for the PC x efficiency data were 100 mV) and are therefore reduced in efficiency.

Table 3.2 summarizes the nominal running voltages for both IC and PC microstrip prints. Note the effect of the lithographic process and geometry on the settings: because the PC prints in general have fewer major defects (and the lithographic defects tend to be less severe), the PC prints are able to hold higher voltage. Furthermore higher voltages are required to produce equivalent gains in the PC prints to that of the IC because of the geometry differences (cf. Table 3.1, Fig. 3.1).

Beam profiles for the MSGC can be compared to drift chamber profiles to ascertain how well the MSGC is performing. Profiles of the incident and scattered beam at the MSGCs are shown in Fig. 3.11a (IC print) and Fig. 3.11b (PC print).

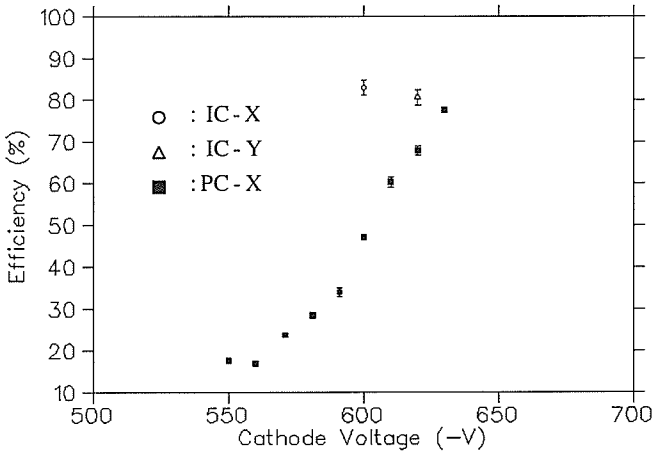

Figure 3.10: An efficiency curve for a PC x print in the D6 area at BNL. Higher voltages were not attained due to sparking on the print. Also depicted are operating points for the IC x and y prints.

Print Type	V_{x_μ} [X-plane] (anode-cathode)	V_{y_μ} [Y-plane] (anode-cathode)	V_d (drift-plane)
IC	600 V	610 V	1500 V
PC	640 V	–	1500 V

Table 3.2: Operating voltages for IC and PC based MSGC during BNL-E885.

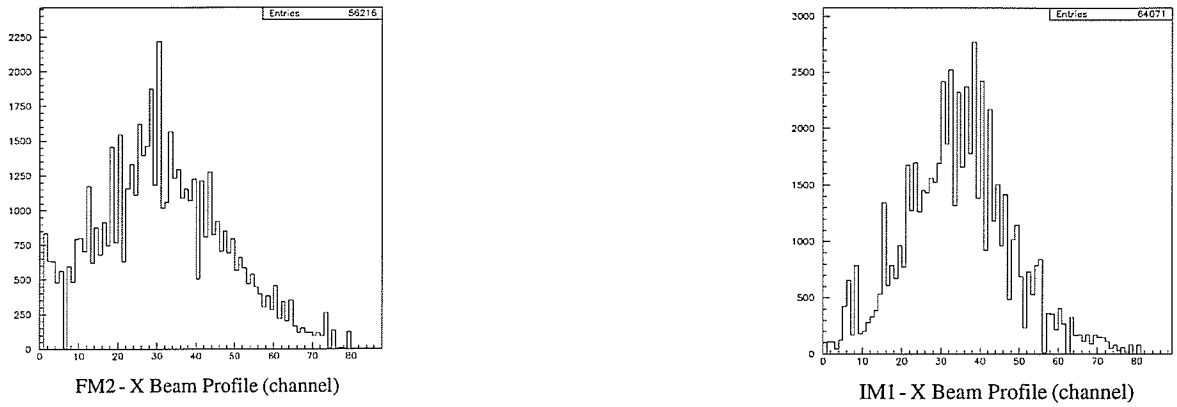

Figure 3.11: a) Beam profile for an IC x (FM2) print at BNL. b) Beam profile for a PC x (IM1) print at BNL.

Seen in the profiles are occasional gaps due to missing anodes. These anodes may be open due to a lithographic defect produced at the time of manufacture, or may have been severed during commissioning. In the latter case, faulty anodes caused sparking and a reduced attainable anode-cathode voltage V_μ, so that the anodes had to be cut ("opened") with a scalpel. In order to compare MSGC profiles with that of the drift chambers, Fig. 3.12 shows a scatterplot of a beamline drift chamber ID3 and the microstrip chamber IM1. Note there is a clear linear correlation with hits in the drift chamber and IM1.

3.8 Discussion

E885 was approved for 1500 hours beamtime, and as such the experiment was completed in the 1996 AGS proton running period. Thus the MSGCs longevity on Large-Hadron Collider (LHC) experimental timescales (in which chambers would ideally run in situ for nearly a decade with little or no intervention) was not an issue. However, deterioration of prints due to sparking and/or modifications in

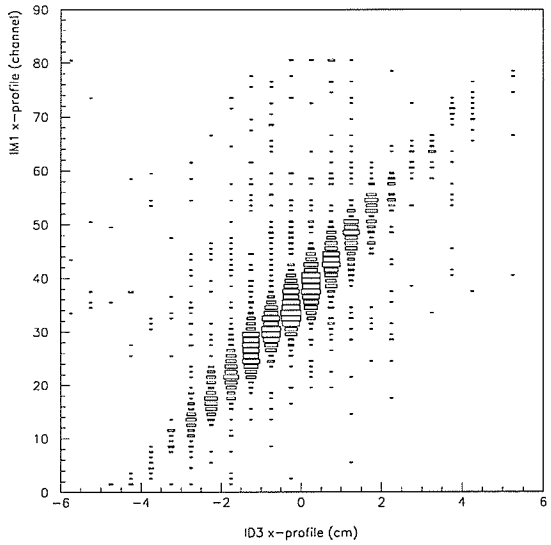

Figure 3.12: Scatter plot of events in an MSGC (IM1) and a drift chamber (ID3), showing correlated hit positions.

gain (possibly due to changes in the passivation layer) were noted.

During the E885 run, the three MSGCs ran with mixed success. Commissioning and running the detectors was arduous, similar in experience to Barr *et al.* [73]. Absolute efficiencies of the detectors were less than desired due to lithographic defects that eliminated some anodes (causing dead regions), and high discriminator thresholds to eliminate external noise sources. In particular, sparking was a constant concern due to the potentially destructive nature of large discharges. Several times in the run, large spark events resulted in "shorts" forming across the anode-cathode gap, tripping the voltage supply. Upon inspection of the print the site of the "short" is visible to the eye, consisting of a large track of carbonization between anode and cathode (Fig. 3.13 is a microphotograph of such a site). Occasionally such sites demanded that an anode be severed and hence resulted in a missing strip when the detector was returned to the beamline. Typically such sparking occurs at the site of lithographic defects. Here the lithographic quality is

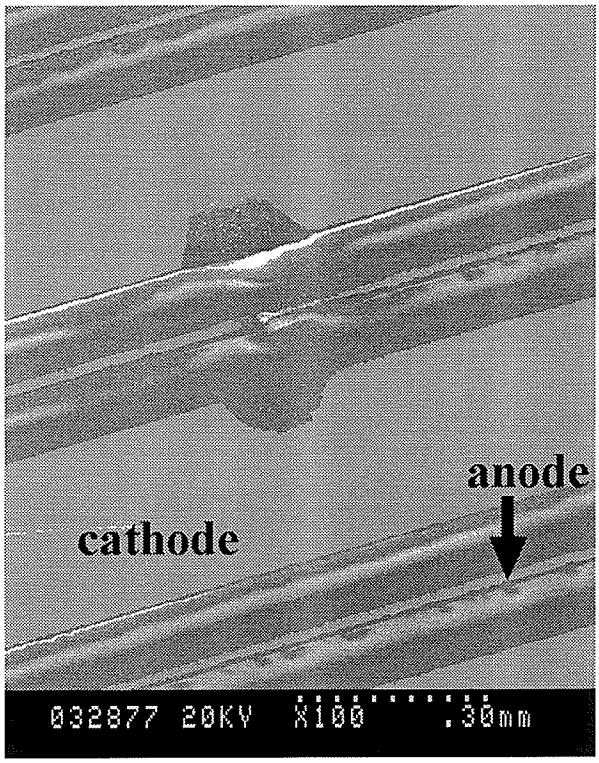

Figure 3.13: Microphotograph of damage due to spark site on an IC print.

poor and irregular, consisting of protuberances or sharp points, causing the electric field to be high and concentrated. This underscores the need for high-quality lithography in both IC and PC processes.

It is imperative to use good shielding and grounding techniques when dealing with high-gain amplifiers such as those required for MSGCs. The detectors have relatively modest gains (10^3 - 10^4) and hence the associated electronics need to be high-gain and will invariably be sensitive to internal and external RF noise.

A recent development at CERN may allow MSGCs to operate at significantly reduced voltages and yet remain ~100% efficient. The Gas Electron Multiplier (GEM) [74, 75] is a composite mesh plane that acts as an avalanche amplifier in gaseous detectors. Placed in the drift volume of an MSGC, two GEM meshes in series can amplify numbers of electrons by up to 10^3, thereby reducing the

operating voltage V_μ of the MSGC, and yet maintaining detector efficiency.

3.9 MSGC summary

E885 marks the first use of PC style prints in an experiment. Efficiencies of the MSGCs reached ~99% in beam tests on sub-sections of microstrip prints, but were reduced in experiment due to localized lithographic defects on prints, and high discriminator threshold settings.

In the future, the issue of longevity of the NiO passivation layer must be studied. Microstrips built with overcoated passivation layers of lead-silicate films have been found to be unstable over long-term usage, perhaps due to thermal or chemical damage produced in high current avalanches [76]. The longevity of MSGCs passivated with metallic oxides will have to be characterized if they are to be candidates in future experiments at the LHC or other high luminosity facilities.

Chapter 4

Data Analysis

4.1 Analysis software

Online and offline data analysis was done using the Interactive Data Analysis package, or IDA [77]. This software, originally developed by the NA36 collaboration at CERN, was modified for use with the experiments on D6-line at BNL by the E813/836 collaboration, while further enhancements were made by the E885 group. IDA provides global section memory, structures for data, and a package for the creation, computing and presentation of histograms. Coding for specific tasks, such us dealing with a particular detector subsystem, was then added to the IDA framework in the form of analyzer routines. Analyzers define and utilize IDA data structures known as SYNOPS.

During the running of the experiment, a subset of the data being written to tape was sent to IDA processes running on Digital Equipment Corporation (DEC) Alpha computers; in this way detector systems and histograms were monitored to ensure proper run conditions prevailed. Offline, IDA was used to skim data tapes for interesting events, and to output multiple streams of specific data to disk files for further analyses. The disk files can be further skimmed using an ntuple analyzer [78] and a subset of SYNOPS written to an *ntuple* data file. An ntuple

is a data structure in which events are recorded, including, for example, specific SYNOPS such as raw detector data, particle momenta, and scattering angles. Ntuples greatly speed data analysis as new cuts can be invoked and investigated, without having to return to disk and refill histograms. The ntuple files were analyzed using the CERN package, Physics Analysis Workstation, or PAW.

4.2 Event reconstruction

4.2.1 Beam particle analysis

Given position information before and after the dipole bending magnet D3 (see Fig. 2.3), an iterative fit can be performed to obtain the momentum of the primary particle, $\mathbf{p}_\mathrm{p}$. Upstream of D3, the beam particle x position is measured by the 72 element hodoscope MP. Downstream of D3, the particle trajectory is formed from position measurements made by ID1-3, and IM1. Particle coordinates in the drift chambers are calculated from hit wire positions, and drift time information, whereas the microstrip chambers use strip position only. Straight-line tracks are then fit to the chambers.

Once the position and track information is known, an iterative fit to calculate the beam particle momentum is performed, using a second order TRANSPORT matrix [79]. If two or more beam tracks are found in the chambers for the event, the so-called "distance of closest approach", or DCA, is used to select the appropriate track. DCA is defined as the minimum distance between two tracks that are intended to be matched (for example, upstream and downstream of D3).

Particle ID is established in the mass slit and incident region. As mentioned earlier, the Čerenkov detector IC vetoes 1.8 GeV/c pions and does not fire for kaons of similar momentum. A time-of-flight (TOF) cut is also made to ensure kaons are selected. A cut is made so that allowed TOF values are consistent with

a 1.8 GeV/c K^- travelling from timing scintillator MT (in the mass slit region) to IT (in the incident region).

4.2.2 Scattered particle analysis

Similar to that of the beam particles, analysis of the scattered (or *secondary*) particle before and after the 48D48 magnet begins with tracking. In the forward region, drift chamber (FD0-2) hit information and drift times are decoded into physical positions. Added to these are hit positions from the microstrip chambers FM1-2, and a least-squares fit is performed to obtain a straight-line track in the forward region. The fringe field of the 48D48 magnet is ignored. Hit information from FD3 (within the magnetic field) is not used at this point in the analysis, with the exception of the formation of the second-level trigger.

Many events include multiple hits in the FD and FM chambers, some of which may be spurious noise, or due to unrelated particles. Hence up to two planes may be dropped by the tracking algorithm when making straight-line fits in the forward region.

In the back region, hits in the 9 planes of the BD chambers are decoded into physical coordinates using hit information and drift times. Straight line fits through the chambers, ignoring the 48D48 fringe field, are performed, allowing up to 2 planes to be dropped.

Tracks from the forward and back regions must be matched, given the known magnetic field of the 48D48, in order to globally reconstruct the path of the secondary particle. To do this, fits through the forward and back chambers, and (x, y) positions at the center of the detectors are passed to an iterative track matching algorithm [50]. Information from the FD3 drift chamber, within the magnetic field of the 48D48 magnet, is also used by the analyzer when matching tracks from the forward and back regions. This routine iteratively calculates

the momentum of the secondary particle via a matrix technique, similar to that of TRANSPORT. The difference is that the acceptance of the spectrometer has been split into 1440 regions; much of the calculation is performed only once at the beginning of the run. The result is to obtain the momentum of the secondary particle, $\mathbf{p}_s$, the pathlength of the secondary particle from $z = 0$ to the BT log it struck, and the goodness of fit.

Goodness of fit is obtained by comparing drift chamber hit information in the forward and back region, to that of the fitted track:

$$\frac{1}{n_x + n_y - n_p}\left[\sum_{i=1}^{5}\left(\frac{(x_{meas} - x_{fit})^2}{\sigma_{ix}^2} + \frac{(y_{meas} - y_{fit})^2}{\sigma_{iy}^2}\right)\right]$$

Here the denominator is the number of degrees of freedom, equal to 5: the number of x and y position measurements, respectively, are $n_x = 5$, and $n_y = 5$ (five measurements of x and y position from the chambers FD1-3 and BD1-2), whereas the number of parameters $n_p = 5$. This definition of goodness of fit is an important variable used to select well-reconstructed events for potential direct $^{12}_{\Xi}$Be production.

4.2.3 Complete event reconstruction

Once tracking is resolved in all regions, i.e. that of the negative particles (typically K^-'s) in the beamline/incident region, and the positive particles (typically K^+'s) in the forward/back regions, and primary and secondary momenta have been established ($\mathbf{p}_p$ and $\mathbf{p}_s$, respectively), event reconstruction can be completed in its entirety. This means generating the vertex position of the interaction, calculating the mass of the secondary particle, m_{sec}, and obtaining the so-called missing mass of the interaction.

Vertex

The minimum distance between the beam particle track and the secondary particle track is denoted DCA, or distance of closest approach. The z value of the DCA segment is taken to be that of the vertex. Given that tracking upstream of the target has fewer sources of error than that of downstream, the (x, y) values of the DCA segment produced by the ID chambers and IM1 are selected for the vertex. Due to imperfect resolution in tracking, DCA is peaked at zero but has a width associated with this resolution.

Secondary and missing mass

The mass of the secondary particle is calculated from time-of-flight (TOF), secondary momentum $\mathbf{p}_\mathrm{s}$, and pathlength. Secondary particle TOF was calculated as the difference of time measurements made at hodoscopes IT and BT, corrected for travel-time of the primary particle from IT to the target. As $\mathbf{p}_\mathrm{s}$ and pathlength have been obtained, the secondary mass is calculated to be

$$m_s = \frac{\mathrm{p_s}}{L/TOF_s}\sqrt{1-\left(\frac{L}{c\cdot TOF_s}\right)^2}. \tag{4.1}$$

The secondary mass is used to select (K^-, K^+) events. We then form what is known in spectrometer-based experiments as the missing mass:

$$\mathrm{M} = \left[((\mathbf{p}_\mathrm{p}^2 + \mathrm{m}_\mathrm{p}^2)^{1/2} + \mathrm{m}_{targ} - (\mathbf{p}_\mathrm{s}^2 + \mathrm{m}_\mathrm{s}^2)^{1/2})^2 - (\mathbf{p}_\mathrm{p}^2 - \mathbf{p}_\mathrm{s}^2)^2\right]^{1/2} \tag{4.2}$$

Here m_{targ} is the mass of the target nucleus, and M may be calculated for m_{targ} equal to the proton mass, or for $\mathrm{m}_{targ} = 11.1749\mathrm{GeV/c}^2$ (quasi-free production on a carbon nucleus). Primary particle mass and momentum are denoted $\mathrm{m_p}$ and $\mathbf{p}_\mathrm{p}$, whereas secondary particle variables are $\mathrm{m_s}$ and $\mathbf{p}_\mathrm{s}$. Missing mass M is thus the invariant mass of the object(s) created in the interaction but not directly detected.

In the (K^-, K^+) events of interest, the primary particle has been identified as a K^-, the secondary particle, as a K^+.

Energy loss in the beamline, target and spectrometer must be accounted for when calculating the missing mass of Equation 4.2. The momentum of the beam particle $\mathbf{p}_p$ tends to be overestimated as the measurement occurs before the particle propagates in the target to the interaction vertex. Energy loss occurs in the primary particle due to coulombic interactions with chamber gases and materials, plastic scintillator material, and the dense carbon target. This energy loss is estimated for 1.8 GeV/c kaons, and subtracted from the primary particle to revise its momentum value. Likewise, the measured momentum of the secondary particle tends to be low, as the measurement occurs after the particle has propagated out of the target and through scintillators, chamber materials and gases. The secondary momentum $\mathbf{p}_x$ is revised upwards by adding back energy losses in the target and chambers.

Energy losses were calculated based on the Bethe-Bloch formalism, with corrections for density effects. The correction for energy loss is simplistic in that it is assumed that the interaction vertex occurs in the center of the target, so that the energy losses assigned for the primary and the secondary particles correspond to travel through one half of the target (about 15 MeV in both cases). Chamber materials contribute another 4.3 MeV (in the primary) and 6.3 MeV (in the secondary) loss in energy.

An event-by-event energy loss correction algorithm was written, but it did not appreciably improve the missing mass resolution. The method was as follows. The interaction vertex was obtained, and primary and secondary tracks were projected to the target face where they entered and exited the target. Pathlengths and energy losses were then established. Momenta were revised and the missing mass was then calculated. However, despite this refinement in the calculation of energy loss and subsequently, the missing mass, the resolution of the spectrometer

remained unchanged. This was an unexpected result. In the original energy loss correction described above, the interaction vertex is assumed to reside at the center of the target. The majority of the energy loss occurs in the target (roughly 75%). Thus it was expected that, with an improvement of vertex resolution due to the addition of the MSGC to tracking, that knowledge of the vertex would yield a better energy loss correction. Issues pertaining to the spectrometer resolution are discussed more fully below, in Section 4.5.2

4.3 Data Reduction

During production running, the diamond target received $0.8 \times 10^{11} K^-$ beam particles. Approximately 190 8 mm data tapes were written, each tape having a capacity of 2.3 Gb (not all tapes were filled, however). The majority of the events written were in fact (K^-, p) events which leaked through FC0 and the second-level trigger. Fig. 4.1 shows the secondary mass distribution for a subset of raw data. Note inelastic and elastic (K^-, p) events comprise over 90% of this raw data. In order to select out the interesting (K^-, K^+) events and produce a more manageable-sized data set, a "reduction" was performed.

Tapes were split into three groups, and distributed to Kyoto University, Carnegie Mellon University, and the University of Manitoba/TRIUMF. An IDA analysis pass of the tape data was performed on DEC OpenVMS Alpha workstations at TRIUMF, applying loose cuts to eliminate (K^-, p) events, and retain (K^-, K^+) ones. Cuts were made on kinematic variables such as the goodness-of-fit, distance of closest approach, the mass of the secondary particle, and the calculated z position of the interaction vertex. This resulted in a much smaller data set which was written to hard disk storage (roughly 2.6 Gb of (K^-, K^+) events from diamond, and 0.3 Gb of (K^-, K^+) events from CH_2). After reducing a respective 1/3 of the data set, each institute distributed the reduced data files, so that all analyses

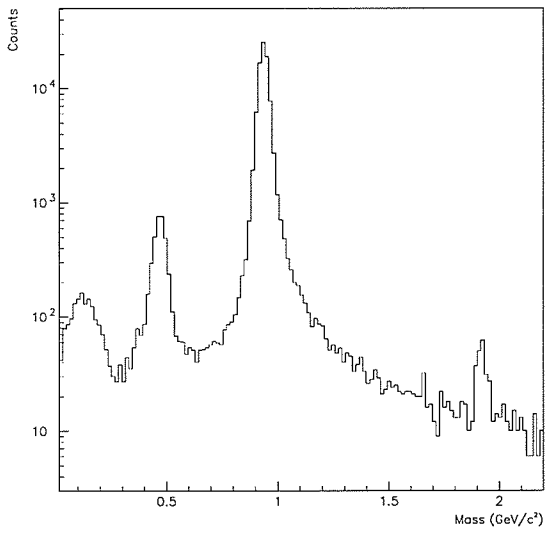

Figure 4.1: Mass distribution for secondary particles for a subset of the raw data. Elastic and inelastic scatter of protons, or (K^-, p) events, comprise over 90% of the raw data set. Peaks in the secondary mass spectrum, from left to right, correspond to the production of π^+ ($m_\pi = 0.140$ GeV/c^2), K^+ ($m_\mathrm{K} = 0.494$ GeV/c^2), protons ($m_\mathrm{p} = 0.938$ GeV/c^2), and deuterons ($m_\mathrm{d} = 1.876$ GeV/c^2).

could use the entire complement of (K^-, K^+) events. After reduction, about 3×10^5 (K^-, K^+) events remain, constituting approximately 10 times the world's previously existing sample of (K^-, K^+) events on carbon. From these events on disk, further studies can be performed and more stringent cuts applied to look for evidence of S=-2 exotic species.

During the reduction phase, several time-of-flight (TOF) calibrations were performed. For instance, an IT-BT TOF calibration was effected on a detector-by-detector, run-by-run basis using protons. This meant a reduction was typically performed twice. First, a reduction was performed on a given run, acquiring statistics for a TOF calibration. The TOF calibration was then performed, ensuring time of flight offsets gave consistent flight times to the back timing wall BT with

respect to predicted TOFs for protons. The run was then re-reduced, using the new TOF offsets.

4.4 MSGC analysis

An existing IDA analyzer was modified to incorporate the microstrip information into particle tracking for the experiment. The software was used to decode hits in the MSGC, make cuts based on timing and time-over-threshold information, convert hits into physical (x, y, z) positions, and do a least-squares fit to hits in drift chamber/MSGC planes to formulate beam and secondary tracks. A matrix inversion technique was used to perform the least-squares fit (see, for example, the discussion in Bevington [80]). Beam and Secondary tracks were then selected on the basis of goodness-of-fit and matched to form an interaction vertex.

In the following sections we review results of the tracking analyzer, such as timing cut issues, position alignment in software, and vertex and energy resolution of the spectrometer.

4.4.1 Timing and pulse width cuts

Analog signals from the MSGC post-amplifier stage (described in Section 3.4) were sent to racks of 33 16-channel discriminators[1]. Signals of sufficient pulse height to fire the discriminator were then passed as an ECL logic pulse to Fastbus 1879 Pipeline TDC modules. Both the time of the pulse arrival, and the time-over-threshold (TOT)[2], were recorded.

[1]Two different makes and models of CAMAC discriminators were used for the MSGC, the Lecroy 4413, and Phillips 7106. Both modules accept analog signals and output ECL logic pulses if the input signal leading edge exceeds a threshold set on the discriminator unit.

[2]The discriminators were operated in a "time over threshold" mode, such that the width of the logic pulse corresponded to the TOT.

In order to eliminate various sources of electronic noise, discriminator thresholds were set higher than optimal, at 80-110mV, depending on the chamber and the plane. Noise levels fluctuated due to a variety of external conditions, necessitating frequent adjustment of threshold levels. Occasionally, noise levels would exceed the hardware threshold set on certain discriminators, causing a series of channels to "ring". Fig. 4.2 is a beam profile from the x plane of FM2, for a subset of the data taken on the carbon target. The beam profile is dominated by a series of ringing channels. The TOT for these events is shown in Fig. 4.3. Events produced by the ringing channels have a very short duration and appear as a spike near zero in Fig. 4.3. These events can be eliminated within the MSGC analyzer by requiring the TOT to be greater than 3 TDC counts.

Not all sources of RF noise exhibited the same time-over threshold behaviour. In some instances, a simple cut on TOT would not eliminate ringing in particular channels or portion of the chamber, as other noise components had different time structures akin to real pulses. In order to maximize good hits passed by the tracking code and eliminate spurious hits in the MSGC, TOT and timing cuts were adjusted on a run-by-run basis. However, for certain periods in the data collection, noise levels in the MSGC would be unchanged, so that TOT and timing cuts would remain constant over those runs. In this case the same cuts are used for the duration of the period of constant running conditions.

Fig. 4.4 shows the same beam profile as in Fig. 4.2, but with a cut to ensure events that pass have a TOT of greater than 3 (TOT$>$ 3). Thus the majority of events in Fig. 4.4 consisted of ringing on four strips. During this period, no pulses due to the passage of charged particles are produced on the four strips, as evidenced by the gaps in the beam profile of Fig. 4.4.

Arrival time information can also be used to eliminate spurious hits in the MSGC. Fig. 4.5 depicts the arrival time of events in the Fastbus 1879 TDCs. Events are cut on the interval $10 < t < 80$, to ensure a good hit in the MGSC. Note

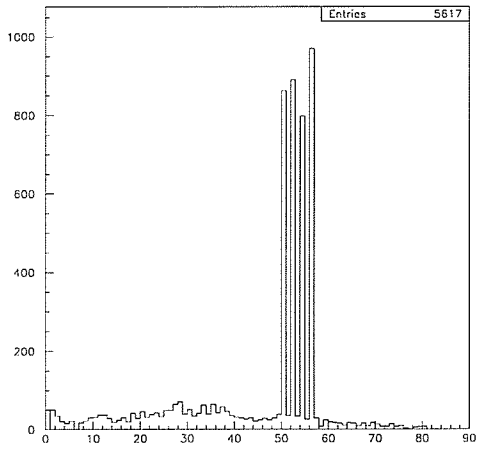

Figure 4.2: Scattered beam profile from the x plane of FM2. Even channels in the range 50-56 are dominated by noise. These even channels correspond to a series of contiguous channels within a QPA02 preamplifier card, wherein even and odd channels are split, largely due to space constraints on the amplifier cards.

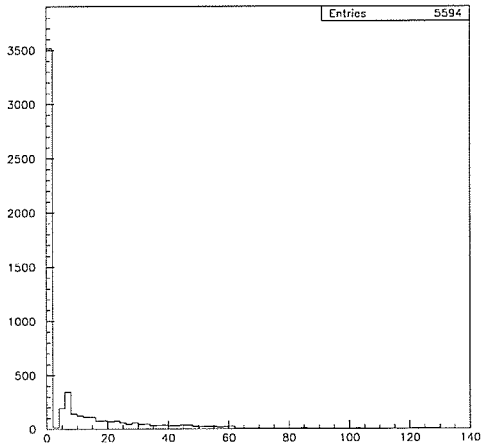

Figure 4.3: Time-over-threshold spectrum for events in the x plane of FM2. Noise events on even channels in the range 50-56 appear as extremely short-duration events near zero.

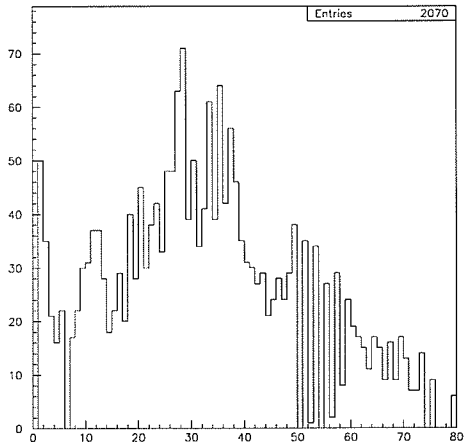

Figure 4.4: The scattered beam profile from the x plane of FM2, shown including a requirement that the time-over-threshold for the event be greater than 3 (TOT> 3).

there is some evidence of cross-talk in the time spectrum of Fig. 4.5, corresponding to the shoulder of the distribution at approximately $50 < t < 60$.

The scattered beam profile from the x plane of FM2, including cuts on the time-over-threshold, and arrival time of the event, is shown in Fig. 4.6

4.4.2 MSGC position alignment

Fine tuning of the position alignment of microstrip planes is performed in software. Data for the alignment run are acquired with the target removed from the area, so that particles follow a straight trajectory after exiting quadrupole Q9 (see Fig. 2.4. Several of these so-called "straight-through" runs were performed during designated calibration periods.

MSGC planes can be positioned in software by a pair of offset parameters, $(x_{\text{off}}, y_{\text{off}})$. A beam track is formulated for particles that traverse the ID chambers.

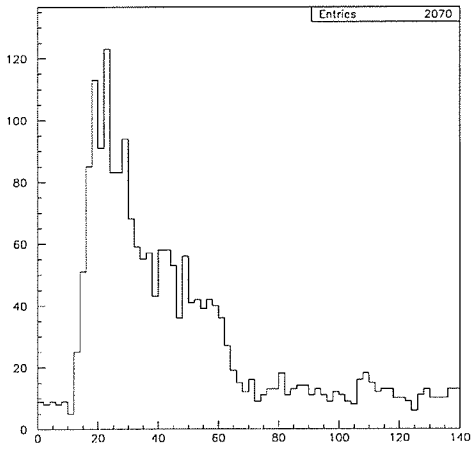

Figure 4.5: TDC spectrum for the x plane of FM2 for a subset of data.

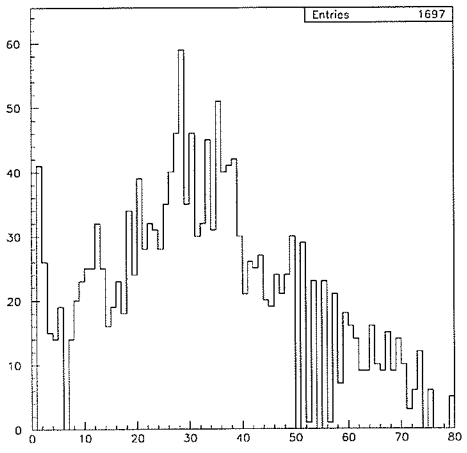

Figure 4.6: Beam profile for the x plane of FM2 for a subset of data, including both arrival time and time-over-threshold cuts.

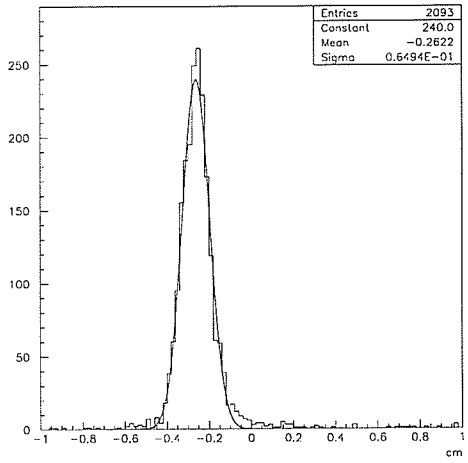

Figure 4.7: Residuals for tracks projected from the ID chambers to the x plane of FM2. A requirement that all nine ID planes are in the fit track is made to maximize the confidence in the projected track. The plane position is erroneously assigned in software.

This track can then be projected by the tracking analyzer to the z-position of a given MSGC plane, and that projected position can be compared to real hits in the plane. A residual is formed when subtracting a projected hit position from a real hit.

As an example of the effect these position offsets have in the tracking software, Fig. 4.7 shows the residuals formed for a sample MSGC plane (FM2-x). A beam track formed from hits in all nine ID planes is projected to the z of FM2-x, and a residual is formed via $x_{\rm proj} - x_{\rm hit}$. Alignment in software is then effected by adjusting $x_{\rm off}$ so that the residual is centered about zero. Fig. 4.8 shows residuals formed after the offset parameter has been modified. This procedure is carried out on all six MSGC planes to obtain a $(x_{\rm off},y_{\rm off})$ pair for each plane.

Once the MSGC have been aligned, they can be incorporated in the tracking for data taken with the carbon target in place. Tracking residuals may also be formed

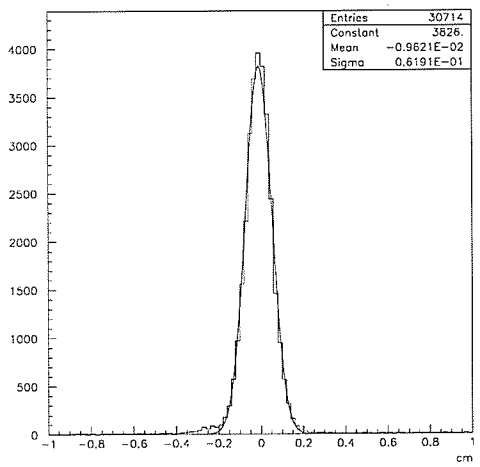

Figure 4.8: Residuals for tracks projected from the ID chambers to the x plane of FM2. The plane has been moved in software, resulting in a fit residual centered at zero.

here; the difference between the predicted and measured position. Residuals for FM1 and FM2 (both x and y planes) are shown in Fig. 4.9.

4.5 Resolutions and the MSGC

4.5.1 Vertex resolution

Fig. 4.10 depicts the z-distribution produced by the tracking analyzer when the MSGC are excluded from the analyses. The z-distribution is obtained by the tracking code by matching beam and secondary tracks and obtaining a vertex; histogramming the z position of reconstructed vertices results in Fig. 4.10. This distribution is a convolution of the solid carbon target ($\Delta z = 50.0$mm), and the position resolution function of the spectrometer and beamline drift chambers. A fit to the histogram is shown, consisting of a convolution of a gaussian distribution ($\sigma = 20$ mm) and a 50 mm solid target. The z-vertex resolution is thus $\sigma = 20$

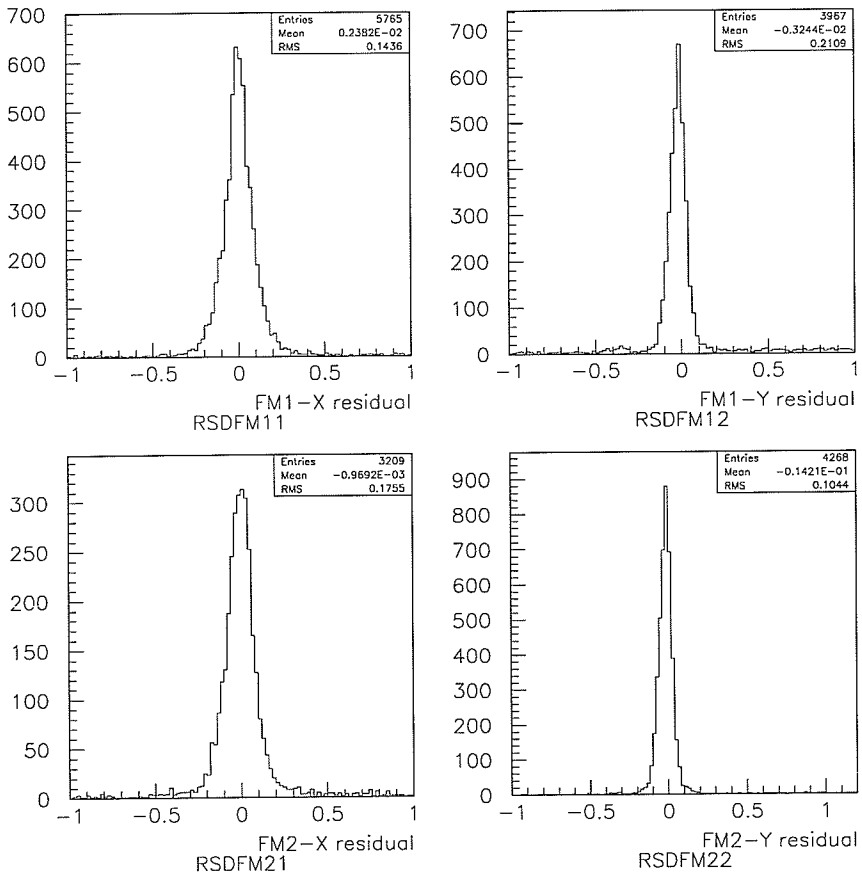

Figure 4.9: Residual distributions for reconstructed tracks in the four microstrip planes downstream of the target, FM1-2, x and y, for a subset of the carbon data. The scale is in cm.

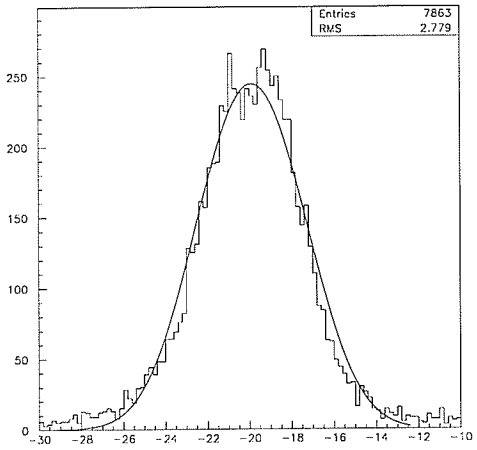

Figure 4.10: Reconstructed z-position of events for a subset of the carbon data. The MSGC are not included in the tracking for this spectrum. A convolution of a gaussian and solid target results in a z-vertex resolution of $\sigma = 20$ mm. The abscissa is in units of cm.

mm

When the MSGC are incorporated into the tracking, the width of the distribution narrows. A convolution of a gaussian ($\sigma = 15$ mm) and a 50 mm solid target is shown. The z-vertex resolution when the MSGCs are included is $\sigma = 15$ mm.

4.5.2 Spectrometer resolution

The energy resolution of the spectrometer can be obtained by direct production of Ξ^- baryons on hydrogen. A polyethylene target, composed of CH_2, provides the hydrogen content, with some carbon contamination. For a series of calibration running periods, the diamond target was removed and replaced with a 130 mm long block of CH_2. Fig. 4.12 depicts the missing mass for several of these calibration runs, where m_{targ} in Equation 4.2 is taken to be the mass of the proton. The

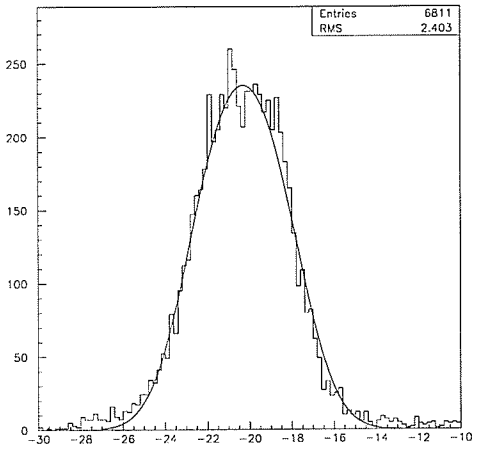

Figure 4.11: Reconstructed z-position of events for a subset of the carbon data. The MSGC have been included in the tracking. A fit to the peak with a gaussian (σ = 15 mm) convolved with a 50 mm solid target is shown. The z-vertex resolution with the MSGCs is thus σ = 15 mm. The abscissa is in units of cm.

histogram includes Ξ^- production on hydrogen (events in the peak), and quasi-free production on carbon in the target (background). Given the Ξ^- is sufficiently narrow (a long-lived state with a mean lifetime of $\tau_{\Xi^-} = (1.639 \pm 0.015) \times 10^{-10}$ s), a fit to the peak will yield the energy resolution of the spectrometer.

In order that the centroid of the peak in Fig. 4.12 coincide with the Ξ^- mass of 1.321 GeV/c^2, a correction factor had to be added into the missing mass calculation. Approximately 30 MeV/c in size, the correction factor was added to the secondary momentum when calculating Equation 4.2. This correction could be handled equally as well by subtracting from the primary particle's momentum the same correction of $\sim$30 MeV/c. This method was employed in the analysis of the H dibaryon search BNL-E836 [27]. However, given the likely cause of this error (2.3%) in missing mass is the imprecision in the magnetic field map of the 48D48 dipole magnet, the correction was applied to the secondary track.

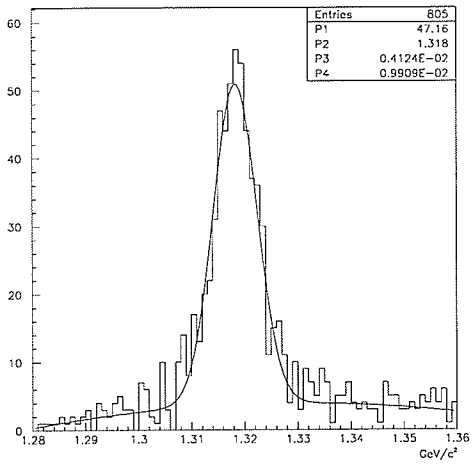

Figure 4.12: Missing mass spectrum for the production of Ξ^- baryons during calibration runs with the 130 mm-long CH_2 target. MSGCs are not included in the tracking. Production on hydrogen appears as a peak, while quasi-free production on the carbon contamination in the target forms a background. A gaussian with $\sigma = 4.1$ MeV is fit to the peak. Background is scaled to quasi-free production on the carbon target (see text).

In order to fit events generated by quasi-free production of Ξ^-'s on carbon (which appears as background in Fig. 4.12), we make use of data from the *carbon* target. A histogram of missing mass, assuming hydrogen kinematics, is obtained for data taken with the carbon target. This spectrum is then fit with a third-order polynomial. Fig. 4.12 is then fit with a linear combination of two functions, i) a gaussian, and ii) a scaled-version of the resulting third-order polynomial fit to the carbon data. A result of the fit is shown in Fig. 4.12. No MSGC were used in generating this spectrum.

Fig. 4.13 is a similar plot, except that MSGC FM1 and FM2 are used in tracking secondary particles. The procedure for fitting the carbon background has been regenerated with the MSGC included. The histogram is then fit with a

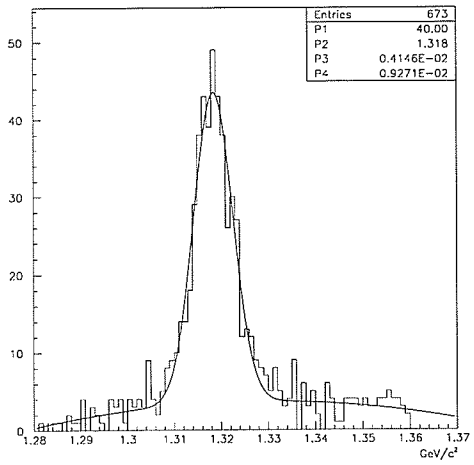

Figure 4.13: Missing mass spectrum for the production of Ξ^- baryons during calibration runs with the 130 mm-long CH_2 target. In this analysis, MSGCs are included in the tracking. A gaussian fit to the peak also yields $\sigma = 4.1$ MeV.

gaussian and a scaled polynomial fit to the carbon data. It appears that the energy resolution is not measurably improved by the addition of the four microstrip planes. The energy resolution of the D6-line spectrometer for E885 was then 4.1 MeV, or 9.7 MeV full-width half-max.

4.6 Excitation energy spectra

The missing mass of Equation 4.2 can be recast as an excitation energy. The excitation energy is essentially the same spectrum as that of missing mass, offset by a particular energy; E_{excit} = M - E_{offset}, where M is missing mass. If E_{offset} is chosen as the sum of the ^{11}B and Ξ^- masses, then bound states will appear below this threshold, in the negative region of an excitation energy spectrum. The negative energy region of the excitation spectrum is kinematically inaccessible to the quasi-free production of Ξ^-'s. Thus, any structure observed below threshold

must be due to exotic S=-2 production as per Equations 1.7-1.9 [3]. Furthermore, if a bound Ξ-hypernuclear state exists, it is expected to appear as a broad peak in the negative excitation energy region. The state is expected to be broad because i) the lifetime will likely be short, and ii) the relatively modest energy resolution of the spectrometer adds to the observed width of the state (For comparison of spectrometer resolutions, the BNL LESB-II beamline and Moby Dick spectrometer has a resolution of ∼2 MeV. However the acceptance of the spectrometer is much lower than that of the 48D48 on D6-line.).

Binding energy is defined as the difference between the mass of the constituent objects, and the mass of the composite object. In the case of Ξ hypernuclei, the binding energy B_{Ξ} is

$$B_{\Xi} = M_{^{A}Z} + M_{\Xi^-} - M_{^{A+1}_{\Xi}(Z-1)}. \tag{4.3}$$

Thus a bound Ξ-hypernuclear state would reside in the negative region of an excitation energy spectrum, and the centroid of that state would yield the binding energy of the Ξ in the nucleus.

4.6.1 Cuts for Ξ-hypernuclei production

Cuts are applied to the analysis of $^{12}C(K^-, K^+)$ data, in order to select particularly clean events. Table 4.1 summarizes the cuts used in the investigation of the binding energy spectrum for evidence of Ξ-hypernuclei.

Two methods were employed in obtaining the cuts of Table 4.1. Certain cuts were selected by visual inspection, to eliminate events in the tail of the distribution while retaining the bulk of the good events. Others were selected on the basis of their effect on what are considered background events; events which occur in the deeply bound region of an excitation spectrum. Cut values which eliminated such

[3] A possible background in the bound region is one Λ in the continuum, and a (yet unobserved) single-lambda hypernucleus such as $^{11}_{\Lambda}$Be.

Cut description	accepted range
secondary mass	0.45 - 0.53 GeV/c^2
goodness of fit (beam track)	0 - 5
goodness of fit (secondary track)	0 - 50
beam momentum reconstructed	true
x vertex	-50 - 50 mm
y vertex	-4 - 4 mm
z vertex	3 σ about z vertex
distance of closest approach (DCA)	0 - 5 mm
BT DCA (x)	-100 - 100 mm
BT DCA (y)	-100 - 120 mm
no. of FD3 planes in fit	4 (all)
IC ADC amplitude	<350 ADC channels
FC ADC amplitude	<350 ADC channels
MTIT time-of-flight (TOF)	within 1ns of kaon TOF
MP TOF	<2ns window of expected TOF
MP elements	only 1-2 hits in 5ns window
ID projection to IT	consistent with hit in IT

Table 4.1: A summary of the cuts used to investigate Ξ-hypernuclei production.

deeply bound events while retaining quasi-free and loosely bound events were employed.

In the following sections, excitation spectra for the carbon data are presented. Several different analyses are performed on the carbon data, but the aim in each is the same: to apply the cuts of Table 4.1 and examine the bound region of the excitation spectrum for evidence of an exotic S=-2 state.

We will consider two sets of the carbon data. The first, Set A, consists of all available experimental runs with the carbon target in place, with essentially nominal conditions (periodically runs were discarded for various reasons including detector and power problems, data acquisition faults and tape drive errors, etc.). The run numbers for the entire carbon data during the E885 data collection period were 2638 - 3043. Note that this range is not contiguous; some runs have been dropped for technical difficulties, others consisted of studies with special trigger mixtures and/or a CH2 target. Set A comprises 234 data runs.

Set B is a subset of A. Set B is composed of only those carbon data runs in which the MSGC chambers were in the beamline and functioning properly (nominal running conditions), runs 2876 - 3043. This subset B consists of 110 data runs, very nearly one-half of the full carbon data set A (despite having less than half the number of runs of Set A, runs during the latter half of the experiment tended to be longer in duration as many earlier problems had been overcome).

When making an analysis pass of the data sets, two different analyses were applied. In the first case, beam and secondary tracks were fit using information from the drift chambers ID1-3 and FD0-3, respectively. Here, information from the MSGC is ignored. In the second case, secondary tracks can be fit using information from both the microstrips FM1-2, and drift chambers FD0-3.

With two data sets to investigate, and two different analysis methods, four excitation energy spectra are produced. In each case, the cuts used to produce the spectra are the same, those of Table 4.1. The spectra are shown in the following

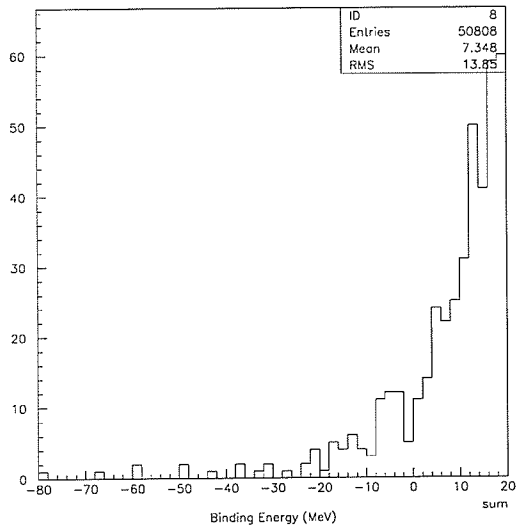

Figure 4.14: Excitation energy spectrum for Set A, without MSGC in the tracking. All carbon data is included.

sections.

4.6.2 Excitation energy spectrum without MSGC

Fig. 4.14 is the excitation energy spectrum for Set A, all carbon data taken in the experiment. The MSGC are not used in the formation of secondary tracks. All cuts from Table 4.1 have been applied.

4.6.3 Excitation energy spectrum with MSGC

Fig. 4.15 is an excitation energy spectrum for Set A, all carbon data taken in the experiment. In this spectrum, MSGC have been included in the tracking. However, here the microstrip chambers FM1-2 have an effect only for those events that occur in the latter half of the carbon data Set A. Data from the first half of Set A do not employ the MSGC. Any improvement of the vertex resolution due to the MSGC will be diluted by the addition of data from the first half of Set A.

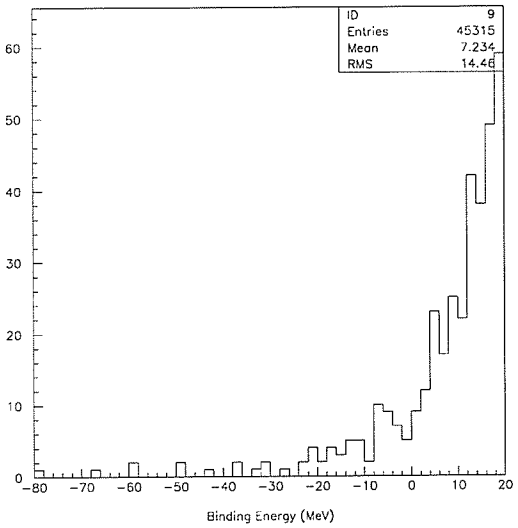

Figure 4.15: Excitation energy spectrum for Set A, with MSGC in the tracking. All carbon data is included. However, the MSGC only have an effect on data taken during the latter half of the experiment.

In Fig. 4.16, excitation energy spectra for a Set B of the carbon data are shown. For comparison, spectra both with and without the MSGC analysis are presented.

A comparison of the number of events in the preceding four spectra, for different regions of excitation energy, is given in Table 4.2. The three regions are loosely defined as 'background' (-80 MeV $<$ E $<$ -40 MeV), 'expected signal' (-20 MeV $<$ E $<$ 0 MeV), and the 'unbound' region (0 MeV $<$ E). The loss of statistics between Sets A and B is due to the MSGC commissioning time. The loss of statistics between analyses with and without the MSGC comes from the lower efficiencies of the MSGC relative to the FD chambers. When the MSGC planes are added in parallel to the FD planes, on average, some events are dropped now due to the addition of somewhat lossy planes.

Comparing ratios of the number of events in the signal region to that of the background, no significant difference is observed between the analyses with and

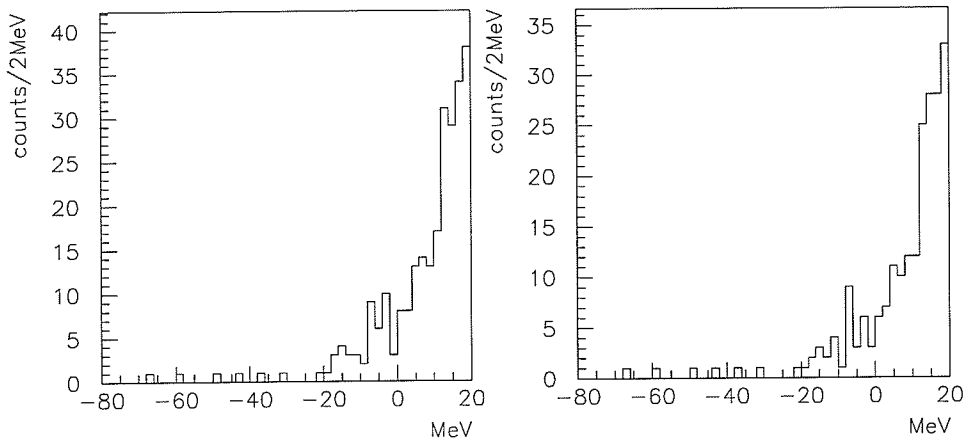

Figure 4.16: Excitation energy spectrum both without (left) and with (right) MSGC included in tracking, for Set B of the carbon data. Runs included are only those for which the MSGC were in place and working nominally. This constitutes about half of the available carbon data set.

E region	description	Set A, no MSGC	Set A, MSGC	Set B, no MSGC	Set B, MSGC
-80 MeV < E < -40 MeV	background	7	7	4	4
-20 MeV < E < 0 MeV	signal	63	52	42	33
0 MeV < E	unbound	50738	45256	29557	25773

Table 4.2: A comparison of the four excitation energy spectra from data sets A and B, with and without MSGC tracking. The number of events in specific energy regions are used for comparison between spectra. No processes are anticipated to contribute to the first (background) region; events are possibly due to misidentified pions or protons. Signal is expected in the second, lightly bound region. Quasi-free production of Ξ^-'s occurs in the third (unbound) region.

without the MSGCs.

4.6.4 Comparison to theoretical estimates

In order to compare the contents of excitation energy spectra to theoretical predictions, the counts of the spectra must be converted to a differential cross-section. This 'normalization' procedure is performed by making use of the differential cross-section of a known reaction. A convenient reaction to use is Ξ^- production on hydrogen, measured by Iijima *et al.* [58].

The procedure consists of two main steps. The first is to normalize the Ξ^- production on hydrogen in the CH_2 target to the known cross section measured by Iijima *et al.* [58]. Next, the quasi-free Ξ^- production on carbon in the diamond target is scaled to agree with quasi-free Ξ^- production via carbon in the CH_2 target. A scaling factor is thus obtained which allows a conversion from counts in the excitation energy spectrum, to differential cross-section.

Details of the normalization method are given in Khaustov [78]. The double-differential cross section of hypernuclear production, averaged over outgoing K^+ angle, is found to be

$$\left\langle \frac{d^2\sigma}{d\Omega dE} \right\rangle^C = A \left(\frac{dN}{dE} \right)_{diam} \tag{4.4}$$

where A is the normalization factor:

$$A = \frac{\alpha^H}{\alpha^C(E)} \frac{\lambda^H_{CH_2}}{\lambda^C_{CH_2}} \frac{N^C_{CH_2}}{N^C_{diam} N^H_{CH_2}} \left\langle \frac{d\sigma}{d\Omega} \right\rangle^H . \tag{4.5}$$

Equation 4.4 relates the angle-averaged differential cross section of Ξ^- production on hydrogen, $\left\langle \frac{d\sigma}{d\Omega} \right\rangle^H$, to the double differential cross section for hypernuclear production on carbon, $\left\langle \frac{d^2\sigma}{d\Omega dE} \right\rangle^C$ (similarly averaged over angle). Definitions of the terms in Equations 4.4 and 4.5 are given in Table 4.3. Numerical values used in the calculation of the normalization factor A are also shown. The angular acceptance over which Equation 4.4 is averaged corresponds to a range of angle θ, the

scattering angle of the outgoing K^+. The maximum K^+ scattering angle allowed is 14°. The acceptances shown in Table 4.3 were calculated in a Monte Carlo simulation by Khaustov [78].

This normalization procedure is convenient in that it is insensitive to differences in reconstruction efficiency between diamond and CH_2 runs. Event reconstruction efficiency is a function of beam intensity; the efficiency suffers during higher intensity runs. The average beam intensity for carbon running periods was about two times that of the CH_2 calibration runs.

The excitation spectrum of Fig. 4.17 includes a scale indicating differential cross-section averaged over $\theta \leq 14°$.

Theoretical predictions for the hypernuclear cross section

Theoretical curves are shown in Fig. 4.17 for the cross section of Ξ hypernuclear production. These curves have been calculated in the framework of the distorted wave impulse approximation (DWIA) by Yamamoto *et al.* [42] at a scattering angle of 0°. In order to make a comparison to the excitation spectrum, the angular dependence and experimental resolution for E885 has been folded in [81].

normalization term	description	value
$\left\langle \frac{d^2\sigma}{d\Omega dE} \right\rangle^C$	angle-averaged double differential cross section for hypernuclear production on carbon	-
$\left(\frac{dN}{dE}\right)_{diam}$	quantity of hypernuclear production events from the diamond target, in an excitation energy interval dE	-
α^H	acceptance for free Ξ^- production on hydrogen, averaged over energy and angle	0.081
$\alpha^C(E)$	acceptance for hypernuclear production on C, as a function of E, angle averaged	0.143
$\lambda^H_{CH_2}$	hydrogen thickness in the CH_2 target (cm^{-2})	10.5×10^{23}
$\lambda^C_{CH_2}$	carbon thickness in the CH_2 target (cm^{-2})	5.25×10^{23}
$N^C_{CH_2}$	number of Ξ^- production events on C in the CH_2 target	317
$N^H_{CH_2}$	number of Ξ^- production events on H in the CH_2 target	377
N^C_{diam}	number of Ξ^- production events on C in the diamond target	45315
$\left\langle \frac{d\sigma}{d\Omega} \right\rangle^H$	differential cross-section of Ξ^- production on H, angle-averaged (μb/sr)	35

Table 4.3: Definitions of terms in the normalization, relating the cross section of the production of free Ξ's on hydrogen, to the hypernuclear production events on carbon.

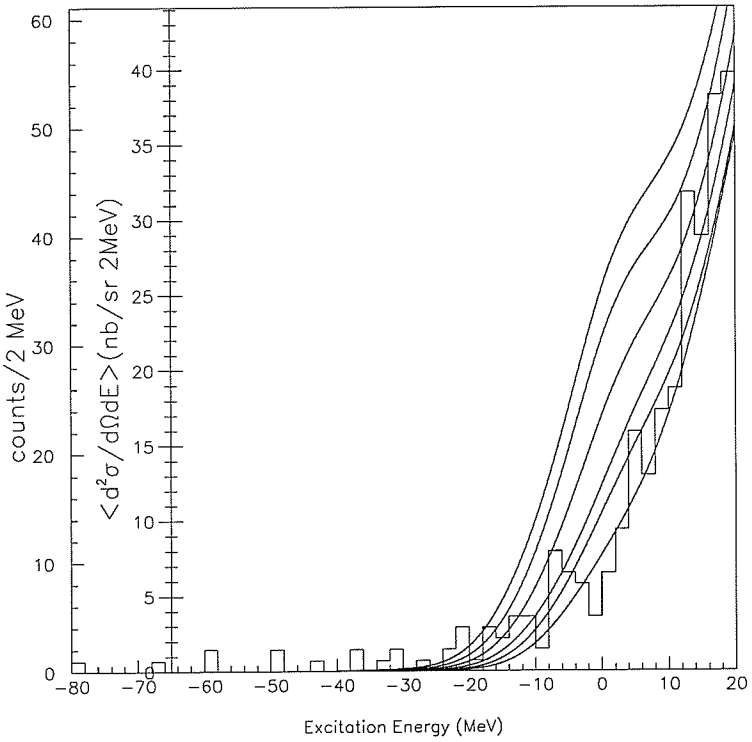

Figure 4.17: Excitation spectrum with MSGCs included in the tracking analysis (this spectrum is the same as Fig. 4.15). The scale of the differential cross section is obtained from the known free production of Ξ^-'s on hydrogen. Additionally, theoretical curves for the production of Ξ hypernuclei, based on different assumptions of $V_{0\Xi}$ are shown. The curves were calculated in the framework of the distorted-wave impulse approximation, assuming (from top to bottom) a $V_{0\Xi}$ of 22, 20, 18, 16, 14 and 12 MeV, respectively.

Chapter 5

Results and Discussion

Experiment 885 was a high statistics experiment that acquired more than 10 times the world's previously existing sample of (K^-, K^+) events on carbon. Approximately 0.8×10^{12} K^-'s incident on a carbon target resulted in 3×10^5 (K^-, K^+) events collected and analyzed. A summary of the results of the experiment, relating to the MSGC, and to the excitation energy spectrum, follows.

Microstrip gas chambers

The MSGC operated in a nominal working mode for the latter half of the E885 data collection period. The vertex resolution of the D6 spectrometer, without the MSGC in place, was 20 mm. The addition of the downstream MSGC FM1 and FM2 improved the vertex resolution to 15 mm. Despite the improvement in position resolution, however, the energy resolution of the spectrometer was not altered and remained 4.1 MeV (r.m.s), for hydrogen kinematics.

The microstrip gas chambers in BNL-E885 employed prints manufactured with two distinct photolithographic processes, IC and PC lithography. The PC x print mounted in IM1 achieved performance consistent with IC counterparts mounted in FM1 and FM2. Due to difficulties in manufacturing, the PC y print was not

available for use during the experiment.

The MSGC proved difficult to commission and run consistently through the data acquisition period. Breakdowns due to sparking, as well as high-current spikes were problematic for most MSGC planes. Similar experiences have been described in the literature, such as the "20 MSGCs" project [73] for the CMS tracker of the Large Hadron Collider (LHC). Experiment 885 was thus one of a handful of experiments to date, that have employed MSGCs. Given the difficulties in running these new detectors for long periods, they have been removed from the designs of some large-scale LHC installations such as ATLAS, and more recently (and controversially), CMS [82]. The future of lithographed position-sensitive detector technology may lie in the gas electron multiplier, or GEM. The GEM is an electron avalanche multiplier and can employ different position readout schemes such as a microstrip print (or variations on MSGC such as the micro-gap [83] or micro-dot [84] detectors) or a conventional wire plane. The addition of one or two GEM planes allows for a significant reduction in the anode-cathode voltage applied to the microstrip print, reducing the potential for sparking. Groundwork in MSGCs, which led to the development of the GEM, may prove instrumental for the future of gaseous position-sensitive detectors.

Ξ-hypernuclei

The excitation energy spectra of Section 4.6, and in particular Figures 4.14 and 4.17, show an excess of events in the bound region. This excess appears to be greater than can be accounted for by limited experimental resolution (i.e. quasi free Ξ production events displaced into the bound region), or a flat background (typically produced by misidentified pions and kaons). Such studies of the potential background were performed in an analysis by Khaustov [78], where it was concluded that the event excess was strong evidence for Ξ hypernuclei. While the event excess in the bound region appears to have structure, this structure is too

narrow, given the modest resolution of the D6 spectrometer (4.1 MeV r.m.s for hydrogen, and with the 50 mm thick carbon target in place, the D6-line energy resolution becomes 6.1 MeV (r.m.s.) [78]). The peak-like shape of the event excess is thus statistical in nature.

Inspecting Figure 4.17 by eye, a Ξ well-depth of 14-16 MeV is favoured over values of 20-22 MeV. This contrasts with the Dover and Gal analysis of emulsion events [1], in which $V_{0\Xi}$ is found to be 21-24 MeV. The value of 14-16 MeV is consistent with the recent result from KEK-E224 [38] noted in Chapter 1, which suggested (despite low statistics) a $V_{0\Xi}$ of 16-17 MeV.

It is conceivable the events in the bound region are due to a hitherto unseen S=-1 hypernucleus, plus a free Λ. The threshold for the production of ${}^{11}_{\Lambda}\mathrm{Be} + \Lambda$ is expected to occur at an excitation energy of approximately -27 MeV. As the production cross section for this process is unknown, no estimate can be made of its contribution to the excitation spectra Fig. 4.17.

Other processes that may produce counts in the bound region include 2-step ones. An example of this is sequential charge-exchange reactions, with the weak force acting between, to project out a state with the appropriate strangeness. For instance, the reaction $K^-\mathrm{p} \rightarrow \overline{K}^0\mathrm{n}$, produces a $\overline{K}^0$, which can oscillate to a K^0. The reaction $K^0\ \mathrm{p} \rightarrow K^+\mathrm{p}$ can then proceed, simulating the double-strangeness exchange reaction. This background was studied for a 7.0 cm CH_2 target, and it was estimated that the 2-step reaction would produce a flat background of approximately 17 events for every 10,000 (K^-, K^+) events on hydrogen. It is thus expected that, for the above reaction, the 2-step contribution to the bound region in the excitation spectrum is minimal [85].

Given several backgrounds potentially feed into the bound region, the value of $V_{0\Xi}$ = 14-16 MeV should be considered as an upper limit on the magnitude of the Ξ well depth. As noted in Section 1.2, an shallow Ξ well depth will preclude the formation of SHM. Depending on the contribution of background processes

to the bound region of the excitation energy spectrum, this limit may indeed be reached. SHM formation may well be precluded, based on a shallow Ξ well depth. However, recall that the process of fitting the tail of the bound region of the excitation spectrum is sensitive to the choice of the radius parameter in the Woods-Saxon formulation. This was not varied for the curves shown in Fig 4.17 ($r_0 = 1.1$ fm), adding further uncertainty to the well depth.

Excitation spectra with and without MSGC were compared. No statistically significant difference between the signal to background ratio of the spectra was noted. Due to the reduced statistics when the MSGC are in place, the number of events that pass the cuts of Table 4.1 was reduced accordingly. A similar fraction of events was then present in the background region, below the excitation energy of about -40 MeV. Thus there does not appear to be an elimination of background events by the MSGC upon their inclusion.

Studies in the field of S=-2 exotic systems will continue in the near future at Brookhaven National Laboratory. However, the focus of strange hadronic physics will likely shift to Japan with the construction of the Japanese Hadron Facility, or JHF. Continuing investigations on the proposed 2 GeV/c beamline there may soon yield definitive information on the nature of matter when several strange quarks are added.

Appendix A

First-Generation Microstrip Gas Chambers

Two prototype microstrip gas chambers were built and tested in 1993-94, in preparation for use in experiment 885. The prototypes are the subject of this appendix. The primary differences between these prototypes and the chambers described in Chapter 3 were: i) the packaging/board layout, and ii) preamplifier cards and electronics.

Microstrip prints used in the two prototypes were the IC prints described in Section 3.2.1. No PC based prints were used in the prototypes (fabrication of PC prints did not occur until 1995-96). Thus, the active area of the first-generation chambers was identical to those used in E885. These prints were sputtered with Ni/NiO in order to eliminate ion deposition on the substrate and subsequent gain degradation of the chamber.

A CAD design of the MSGC board layout is shown in Fig. A.1. The MSGC main board was designed to accept the same 80×50 mm^2 print, hence the dimensions are similar to the MSGC of Chapter 3. The MSGC were expected to be interleaved in a segmented target and as such, there existed a requirement that they be very thin in the z direction, no more than 10.0 mm thick. As the

chamber incorporated two microstrip prints back-to-back (an x and a y print), the gas volume had to be exceptionally narrow in the z direction. In order to achieve this narrow volume, the chamber windows, made of aluminized mylar, also acted as the drift plane electrode for the MSGC. The inner surface of the chamber window was aluminized and held at a potential of -1.5 kV. The gas gap was then approximately 3 mm (a slight bowing of the chamber windows under gas meant the gap was slightly greater than 3 mm). The drift planes were able to maintain voltage indefinitely and did not suffer from arcing problems, despite doubling as a window. However some stray electric field was present outside the chamber window, as noted by the accumulation of dust particles on the exterior.

The preamplifier employed by the prototypes was a single-channel charge-to-voltage amplifier designed by G.H. Coombes of TRIUMF, denoted USCPA1. Originally fabricated for the HERMES experiment at DESY [63] as a multi-channel monolithic preamp card, single channels were separated onto 15 mm $\times$ 43 mm $\times$ 0.5 mm wafers. The USCPA1 had a charge gain of 25 mV/fC, an equivalent noise charge of 2000 electrons, and a shaping time of 40 ns.

Fig. A.2 is an image of one of the prototypes being benchtested at Brookhaven National Laboratory. The USCPA1 single-channel amplifier cards are situated normal to the MSGC main board, clustered about the microstrip print enclosure to ensure a small path length for unamplified signals. Amplified signals were sent on 30' twisted-pair cable to a series of N-277 16 channel differential input amplifier/discriminator cards built by Nanometric Systems Inc..

Bench and beam tests were performed at both TRIUMF and Brookhaven lab. The tests were similar in nature to those described in Chapter 3. In Fig. A.3, efficiency measurements performed at the M13 beamline of TRIUMF are shown. Efficiencies were measured for both x and y prints. In both cases, a sixteen-channel subset of a given print was instrumented and tested (two such subsections were utilized on the y print). The efficiency measurements were performed by taking

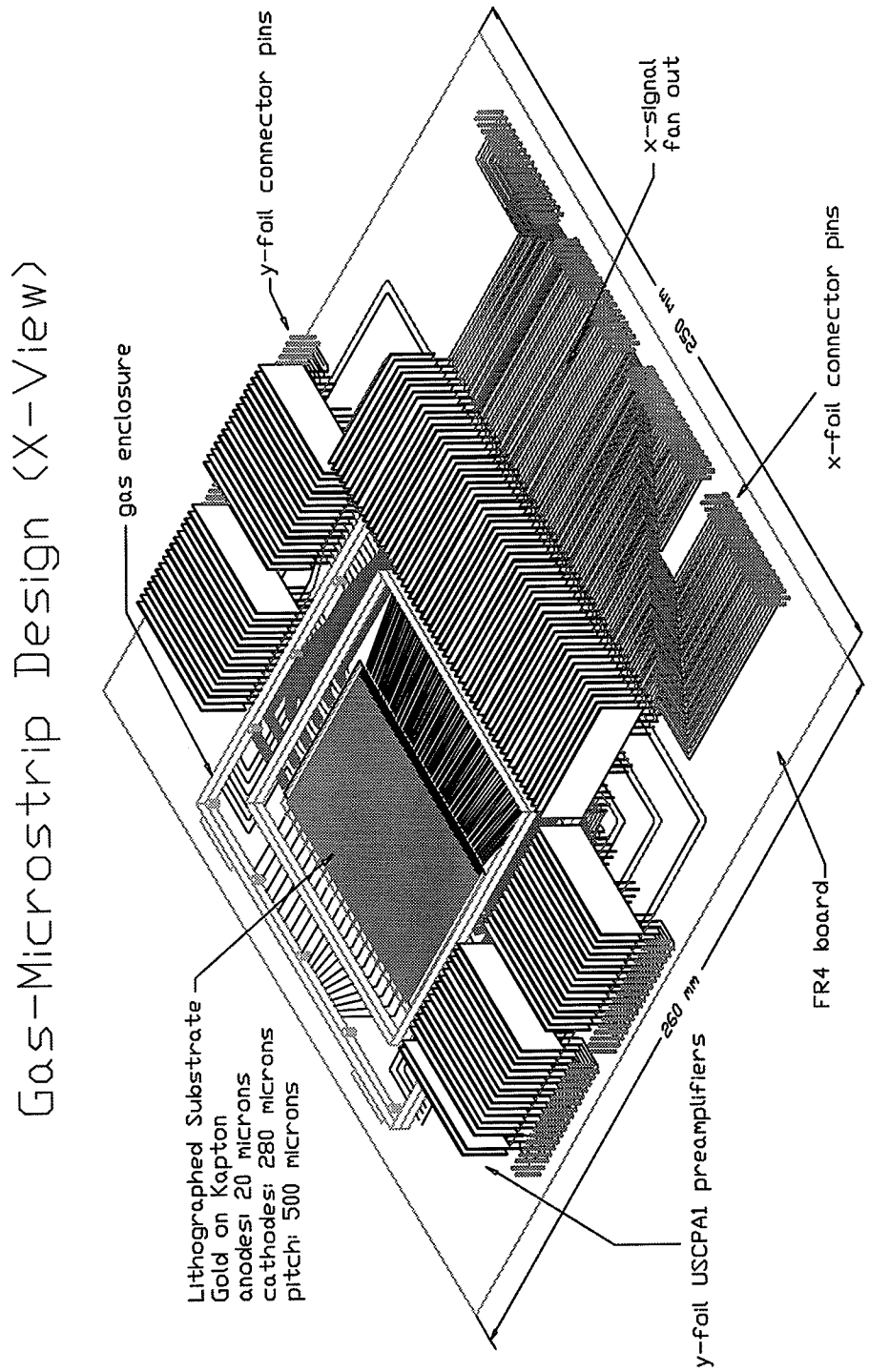

Figure A.1: Schematic of the first-generation MSGC.

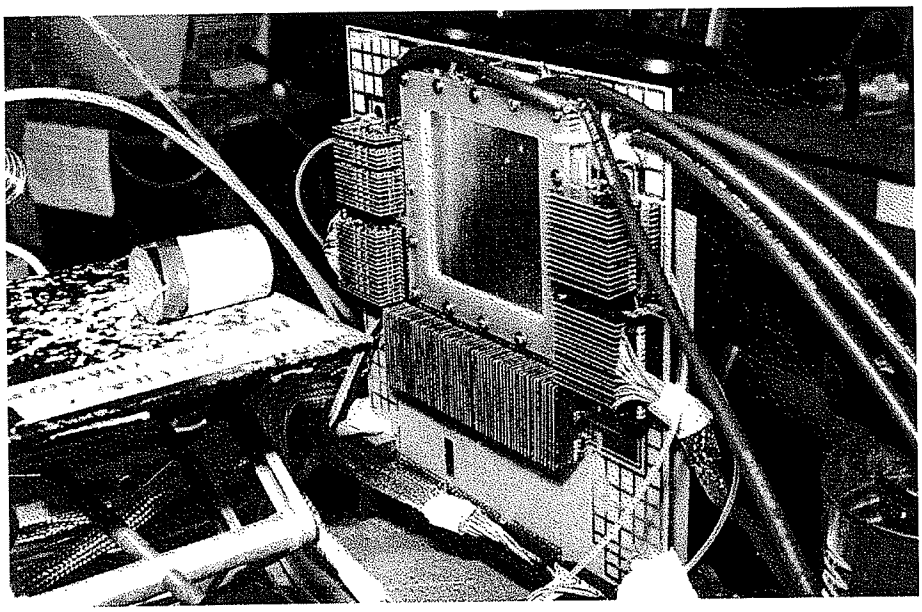

Figure A.2: One of the two prototypes under benchtesting at Brookhaven National Laboratory. Situated in front of the enclosure window is a 1 mCi ^{55}Fe source.

the ratio of events in the subset of anodes to the number of trigger signals as defined by two small scintillators (5 mm $\times$ 5 mm) placed in front of and behind the MSGC. The gas used in these measurements was Argon/Isobutane (90:10).

The prototype MSGC gave an understanding of how the nickel-coated IC prints would behave in a beam of minimum ionizing particles, and what efficiencies could be anticipated from the chambers. However, the electronics of the second generation MSGC were substantially different, leading to different challenges with respect to noise pickup. Results of the tests on the MSGC prototypes were presented at an international workshop on microstrip chamber development [86].

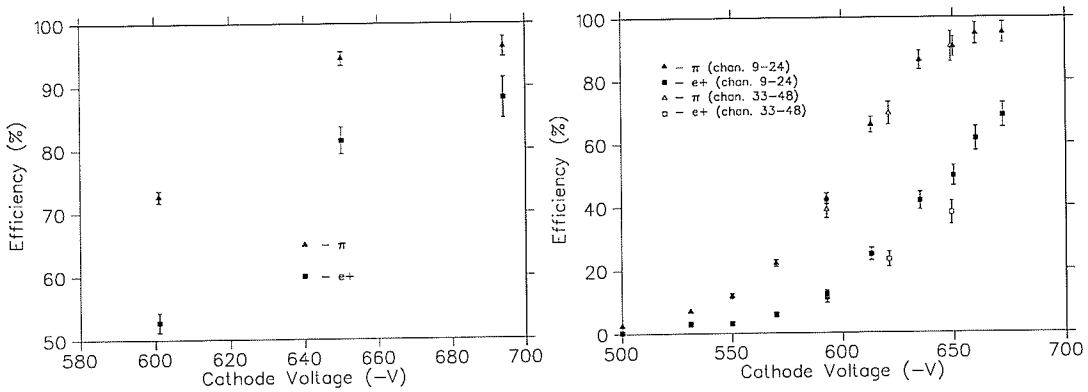

Figure A.3: a) Absolute efficiency curve for a subset of the x print of an MSGC prototype. b) Absolute efficiency curve for two different subsections of the y print of an MSGC prototype.

Bibliography

[1] C.B. Dover and A. Gal. *Ann. Phys.*, 146:309, 1983.

[2] L. Leprince-Ringet and M. L'héritier. *Comptes Rendus Acad. Sciences de Paris, séance du 13 Dec. 1944*, page 618, 1944.

[3] G.D. Rochester and C.C. Butler. *Nature*, 160:885, 1947.

[4] M. Gell-Mann. *Phys. Rev.*, 92:833, 1953.

[5] T. Nakayo and K. Nishijima. *Prog. Theor. Phys.*, 10:581, 1953.

[6] K. Nishijima. *Prog. Theor. Phys.*, 13:285, 1955.

[7] R.N. Cahn and G. Goldhaber. *The Experimental Foundations of Particle Physics.* Cambridge University Press, 1989.

[8] V.E. Barnes *et al. Phys. Rev. Lett.*, 12:204, 1964.

[9] C. Greiner and J. Schaffner-Bielich. Physics of strange matter. In R. K. Gupta and W. Greiner, editors, *Heavy Elements and Related New Phenomena*, page 1, World Scientific Publications, 1998.

[10] R.E. Chrien and C.B. Dover. *Ann. Rev. Nucl. Part. Sci.*, 39:113, 1989.

[11] B. Povh. *Prog. Part. Nucl. Phys.*, 18:183, 1987.

[12] H. Bandō, T. Motoba, and J. Žofka. *Int. J. Mod. Phys.*, A5:4021, 1990.

[13] J.K. Tuli. Nuclear wallet cards. Brookhaven National Laboratory, New York, 1995. Appendix V.

[14] A.R. Bodmer. *Phys. Rev. D.*, 4:1601, 1971.

[15] R.L. Jaffe. *Phys. Rev. Lett.*, 38:195, 1977.

[16] M. May. Proceedings of the international conference on hypernuclear and strange particle physics. *Nucl. Phys.*, A639:363, 1998.

[17] M.M. Nagels *et al. Phys. Rev. D*, 15:2547, 1977.

[18] M.M. Nagels *et al. Phys. Rev. D*, 20:1633, 1979.

[19] G. Franklin. Proceedings of the international conference on hypernuclear and strange particle physics. *Nucl. Phys.*, A585:83, 1995.

[20] J. Schaffner, C.B. Dover, A. Gal, C. Greiner, and H. Stöcker". *Phys. Rev. Lett.*, 71:1328, 1993.

[21] J. Schaffner, C.B. Dover, A. Gal, D.J. Millener, C. Greiner, and H. Stöcker. *Ann. Phys.*, 235:35, 1994.

[22] A. Gal. private communications.

[23] M. Danysz *et al. Phys. Rev. Lett.*, 11:29, 1963.

[24] D.J. Prowse. *Phys. Rev. Lett.*, 17:782, 1966.

[25] S. Aoki *et al. Prog. Theor. Phys.*, 85:1287, 1991.

[26] C.B. Dover, D.J. Millener, A. Gal, and D.H. Davis. *Phys. Rev. C.*, 44:1905, 1991.

[27] R.W. Stotzer. PhD thesis, The University of New Mexico, Albuquerque, NM, USA, 1997.

[28] R.W. Stotzer *et al. Phys. Rev. Lett.*, 78:3646, 1997.

[29] J.K. Ahn *et al.* Proceedings of the international conference on hypernuclear and strange particle physics. *Nucl. Phys.*, A639:379, 1998.

[30] A. Ohnishi, Y. Hirata, Y. Nara, S. Shinmura, and Y. Akaishi. nucl-th/9903021.

[31] The BNL-E813 Collaboration, to be submitted for publication.

[32] P.H. Steinberg and R.J. Prem. *Phys. Rev. Lett.*, 11:429, 1963.

[33] S. Aoki *et al. Prog. Theor. Phys.*, 89:493, 1993.

[34] D.H. Wilkinson *et al. Phys. Rev. Lett.*, 3:397, 1959.

[35] J. Catala *et al.* Proceedings of the international conference on hypernuclear physics. 2:758, 1969.

[36] A.S. Mondal *et al. Nuovo Cim.*, 54A:333, 1979.

[37] A. Bechdolff *et al. Phys. Lett.*, 26B:174, 1968.

[38] T. Fukuda *et al. Phys. Rev. C*, 58:1306, 1998.

[39] Y. Yamamoto. *Few-Body Syst. Suppl.*, 9:145, 1995.

[40] A. Gal. private communications.

[41] K. Ikeda *et al. Prog. Theor. Phys.*, 91:747, 1994.

[42] Y. Yamamoto *et al. Prog. Theor. Phys. Suppl.*, 117:281, 1994.

[43] D.J. Millener *et al. Prog. Theor. Phys. Suppl.*, 117:307, 1994.

[44] M.M. Nagels, T.A. Rijken, and J.J. deSwart. *Phys. Rev. D*, 12:744, 1975.

[45] C.B. Dover and A. Gal. *Prog. Part. Nucl. Phys.*, 12:171, 1984.

[46] R. Sawafta *et al.* Proceedings of the international conference on hypernuclear and strange particle physics. *Nucl. Phys.*, A639:103, 1998.

[47] P.H. Pile, D. Beavis, R.L. Brown, R. Chrien, G. Danby, J. Jackson, D.M. Lazarus, W. Leonhardt, C. Pearson, A. Pendzick, P. Montemurro, T. Russo, J. Sandberg, R. Sawafta, C. Spataro, and J. Walker. *Nucl. Instr. and Meth.*, A 321:48, 1992.

[48] AGS Proposal E885, Spokespersons C. Davis, G.B. Franklin and M. May.

[49] D. Zhu, C.B. Dover, A. Gal, and M. May. *Phys. Rev. Lett.*, 67:2268, 1991.

[50] F. Merrill. PhD thesis, Carnegie Mellon University, Pittsburgh, PA, USA, 1995.

[51] A. Oed. *Nucl. Instr. and Meth.*, A 263:351, 1988.

[52] M. Burger. PhD thesis, University of Freiburg, Freiburg, Germany, 1996.

[53] T. Bürger. PhD thesis, University of Freiburg, Freiburg, Germany, 1997.

[54] T. Iijima. PhD thesis, Kyoto University, Kyoto, Japan, 1995.

[55] V. Sum *et al. Nucl. Instr. and Meth.*, A 326:489, 1993.

[56] L. Gan. PhD thesis, University of Manitoba, Winnipeg, MB, Canada, 1998.

[57] P. Khaustov *et al.* Published in *Phys. Rev. C*, Volume 61, Feb. 2000.

[58] T. Iijima *et al. Nucl. Phys.*, A 546:588, 1992.

[59] D.E. Alburger and M. May. to be published in Nucl. Instr. and Meth.

[60] M.R. Landry, J. Birchall, C.A. Davis, W. Faszer, L. Gan, L. Lee, S.A. Page, W.D. Ramsay, M. Salomon, and W.T.H. van Oers. *Nucl. Instr. and Meth.*, A 421:31, 1999.

[61] F. Angelini, R. Bellazzini, A. Brez, G. Decarolis, C. Magazzù, M.M. Massai, G. Spandre, and M.R. Torquati. *Nucl. Instr. and Meth.*, A 315:21, 1992.

[62] M.H.J. Geijsberts *et al.* NIKHEF-H/94-12, 1994. cited in ref. [65].

[63] K. Ackerstaff *et al. Nucl. Instr. and Meth.*, A 417:230, 1998.

[64] A. Oed. *Nucl. Instr. and Meth.*, A 367:34, 1995.

[65] F. Sauli. *Nucl. Phys. B (Proc. Suppl.)*, 61B:236, 1998.

[66] J.H. Moromisato. *Nucl. Instr. and Meth.*, A 345:90, 1994.

[67] M. Salomon, K. Crowe, W. Faszer, P. Lindsay, and J.M. Curran Maier. *IEEE Trans. Nucl. Sci.*, NS-43:1157, 1996.

[68] R. Bouclier, M. Capeáns, G. Million, L. Ropelewski, F. Sauli, T. Temmel, R.A. Cooke, S. Donnel, S.A. Sastri, and N. Sonderer. *Nucl. Instr. and Meth.*, A 369:328, 1996.

[69] A. Barr, R. Bouclier, M. Capeáns, G. Della Mea, M. Hoch, G. Million, G. Manzin, L. Ropelewski, and F. Sauli. *Nucl. Instr. and Meth.*, A 392:99, 1997.

[70] M. Salomon, J. Armitage, G. Chapman, M. Dixit, J. Dubeau, W. Faszer, L.A. Hamel, and G. Oakham. *Nucl. Instr. and Meth.*, A 351:313, 1994.

[71] T.Zimmerman. *IEEE Trans. Nucl. Sci.*, NS-37:439, 1990.

[72] R.J. Yarema and T.Zimmerman. *IEEE Trans. Nucl. Sci.*, NS-37:430, 1990.

[73] A. Barr, S. Bachmann, B. Boimska, R. Bouclier, A. Braem, C. Camps, M. Capeáns, V. Commichau, W. Dominik, G. Flügge, F. Gómez, R. Hammarstrom, K. Hangarter, M. Hoch, J.C. Labbé, D. Macke, G. Manzin, F. Meijers, G. Million, K. Muhlemann, V. Nagaslaev, A. Peisert, L. Ropelewski, O. Runolfsson, F. Sauli, R. Schulte, M. Schulz, A. Sharma, L. Shekhtman, and C. Wolff. *Nucl. Instr. and Meth.*, A 403:31, 1998.

[74] C. Büttner, M. Capeáns, W. Dominik, M. Hoch, J.C. Labbé, G. Manzin, G. Million, L. Ropelewski, F. Sauli, and A. Sharma. CERN-PPE/97-73.

[75] R. Bouclier, W. Dominik, M. Hoch, J.C. Labbé, G. Million, L. Ropelewski, F. Sauli, A. Sharma, and G. Manzin. *Nucl. Instr. and Meth.*, A 396:50, 1997.

[76] R. Bouclier, M. Capeáns, C. Garabatos, G. Manzin, G. Million, L. Ropelewski, F. Sauli, E. Shefer, L. Shekhtman, T. Temmel. G. Della Mea, G. Maggioni, and V. Rigato. In Progetto, editor, *Proc. Int. Workshop on Micro-Strip Gas Chambers, Legnaro, 1994*, page 39, Padova, 1995.

[77] I.R. Sukaton. PhD thesis, Carnegie Mellon University, Pittsburgh, PA, USA, 1995.

[78] P. Khaustov. PhD thesis, Carnegie Mellon University, Pittsburgh, PA, USA, 1999.

[79] K.L. Brown, F. Rothacker, D.C. Carey, and Ch. Iselin. *CERN Report*, 80-04:1, 1980.

[80] P.R. Bevington. *Data Redutcion and Error Analysis for the Physical Sciences.* McGraw-Hill, 1969.

[81] K. Yamamoto. private communications.

[82] F. Sauli. private communications.

[83] F. Angelini *et al. Nucl. Instr. and Meth.*, A 349:412, 1994.

[84] S.F. Biagi *et al. Nucl. Instr. and Meth.*, A 361:72, 1995.

[85] G. Franklin. private communications.

[86] M. Landry, J. Birchall, K. Crow, C.A. Davis, W. Faszer, L. Gan, L. Lee, S.A. Page, W.D. Ramsay, M. Salomon, and W.T.H. van Oers. In Progetto, editor, *Proc. Int. Workshop on Micro-Strip Gas Chambers, Legnaro, 1994*, page 132, Padova, 1995.